arXiv:1701.00463v2 [physics.flu-dyn] 22 Jan 2017

Free-Surface Enthalpy Method for Transient Convection/Diffusion Phase Change

Amirsaman Farrokhpanah*[1], Javad Mostaghimi[1], and Markus Bussmann[1]

[1]*Department of Mechanical & Industrial Engineering, University of Toronto, Toronto, Canada*

Abstract

A three-dimensional model is developed for prediction of solidification behavior using non-linear transformation of the enthalpy equation in Smoothed Particle Hydrodynamics (SPH) discretization. Effect of phase change in the form of release and absorption of latent heat is implemented implicitly as variable source terms in the enthalpy calculations. Developed model is validated against various experimental, analytical, and numerical results from literature. Results confirm accuracy and robustness of the new procedures. Finally, the improved SPH model is applied to study of Suspension Plasma Spraying (SPS) by predicting impact and solidification of molten ceramic droplets on the substrate. These cases include predictions for spread factor and splat formation depending on impact velocities and temperatures. This application helps in identification of different processes involved in the SPS coating process.

Keywords: SPH, Phase Change, Suspension Plasma Spraying

Nomenclature

C	Heat capacity
H	Enthalpy
k	Thermal conductivity
L	Latent heat
l	Liquid state (subscript)
m	Mushy state (subscript)
s	Solid state (subscript)
T	Temperature
t	Time
T^*	Kirchhoff temperature
t^*	Non-dimensional time
T_1	Alloy lower melting temperature
T_2	Alloy upper melting temperature
T_m	Melting temperature

*farrokh@mie.utoronto.ca

1 Introduction

Coating is the process of covering a surface with particular materials with the goal of protection or forming more advanced materials. Thermal spraying, one of the examples of the coating process, uses heat from combustion or electrical arc to melt solid materials. These molten droplets are then accelerated using gas jet to impact a destination substrate and solidify on its surface. An interesting type of thermal spray is the Suspension Plasma Spraying (SPS) process. SPS is emerging as a powerful coating technique for depositing high quality thermal barrier coatings. Fine ceramic powders are used for creating stable suspensions. The solvent can be fluids such as water or ethanol. The heat from plasma evaporates this carrier fluid and then melts the solid matter. The molten particles will then impact the substrate at high velocities and solidify.

Solidification is undoubtably an important part of many coating processes. Finite Volume method followed later by Finite Element [1] have been typically used for numerical study of phase change. Usage of Smoothed Particle Hydrodynamics (SPH) has also been recently suggested by several studies. High computation efficiency through parallelization capability, and the ability of handling complex geometries is among the main advantages of this method. It has also been successfully used for simulation of different physical phenomena such as tsunami simulations [2], simulation of floating bodies like ships [3], atomization of liquid jets [4], impact of liquid drops over surfaces [5], and other multiphase studies [6, 7, 8].

The amount of heat needed for the phase change process to take place is called the latent heat. This heat is absorbed (released) during solidification (melting) at a constant temperature for pure materials and over a temperature range for alloys. Inclusion of this process into the numerical models demands making modifications to heat transfer calculations. This is either done by adding the heat as a source term, like the works of Passandideh [9] and Voller [10], or by modifying heat capacity coefficient, as in the works of Thomas et al. [11], Hsiao [12], and Dalhuijsen et al. [1]. Inclusion of latent heat in SPH formulation by modification of the heat capacity coefficient has been already performed in an study by Farrokhpanah et al. [13]. Addition of source term in energy formulation of SPH still remains an open topic.

Common practice in previous studies is explicit inclusion of latent heat as a post processing step in solving energy equation, as in the works of Cleary et al. [14, 15]. This model has been applied to different studies such as casting [16] and droplet solidification [17, 18, 19]. As an alternative, Monaghan et al. [20] suggested modeling solidification of pure and binary alloys using a stationary grid of ghost particles. The drawback of this procedure is the need for extra particles resulting in implementation difficulties.

Here, a new procedure is introduced in SPH discretization by non-linear transformation of the enthalpy equation for handling transient convective phase change problems, inspired by the work of Cao et al. [21]. As it will be shown later, benchmark of the resulting formulation against various analytical and numerical results proves robustness of the procedure. The latent heat here will appear implicitly as a source term in the energy calculations and can be reliably applied to free surface convective problems. As an example, application of the new model is shown here for study of impact and solidification of sub-micron ceramic droplets generated during Suspension Plasma Spraying. Condition of droplets upon impact, i.e. impact location, velocity, temperature, and diameter, has been obtained from a previous study of ours available in [22], and is referenced throughout this paper as the 'SPS data'.

2 Governing equations

2.1 Lagrangian Navier-Stokes equations

Navier-Stokes equations in a Lagrangian framework are

$$\frac{D\rho}{Dt} = -\rho\nabla.v \tag{1}$$

$$\frac{Dv}{Dt} = \frac{1}{\rho}[-\nabla p + \mu\nabla^2 v + F^{st} + F^b] \tag{2}$$

where F^b represents external body forces such as gravity and F^{st} is the surface tension force. These equations are closed by equation of state, which calculates pressure using density in the form of [23]

$$P = P_0(\frac{\rho}{\rho_0})^\gamma + b \tag{3}$$

where $\gamma = 7$ and 1.4 for liquid and gas phases, respectively, b is a background pressure, and P_0 represents a reference pressure adjusted to keep maximum density deviations from ρ_0 in the order of O(1%) [23].
Applying integral interpolation to continuity and Navier-Stokes equations

$$\frac{D\rho_i}{Dt} \cong \sum_{j=1}^{N} m_j(\mathbf{v_i} - \mathbf{v_j}) \cdot \nabla_i W \tag{4}$$

$$\frac{D\mathbf{v_i}}{Dt} \cong -\sum_{j=1}^{N} m_j(\frac{p_i}{\rho_i^2} + \frac{p_j}{\rho_j^2})\nabla_\mathbf{i} W + 4m_j \left(\frac{(\mu_i + \mu_j)\mathbf{x_{ij}} \cdot \nabla_\mathbf{i} W}{(\rho_i + \rho_j)^2 |\mathbf{x_{ij}}|^2}\right) \mathbf{v_{ij}} + \frac{\mathbf{F_{ij}^{st}}}{m_i} + \mathbf{F^b} \tag{5}$$

where m is the mass of each particle. To avoid possible singularities, it is beneficial to expand $\frac{\mathbf{x_{ij}} \cdot \nabla_\mathbf{i} W}{|\mathbf{x_{ij}}|^2}$ before calculations and remove a position vector that appears in both denominator and numerator, which can become close to or equal to zero.
Surface tension is calculated by applying interaction forces among particles in the form of [24]

$$\mathbf{F_{ij}} = \begin{cases} S_{ij} cos(\frac{1.5\pi}{3h}|\mathbf{x_{ij}}|)\frac{\mathbf{x_{ij}}}{|\mathbf{x_{ij}}|} & |\mathbf{x_{ij}}| \leq h \\ 0 & |\mathbf{x_{ij}}| > h \end{cases} \tag{6}$$

between each i and j particles. S_{ij} is a constant that controls the magnitude of surface tension force between each phase. Contact angles and interactions between fluids and solids can be obtained by choosing different values for S_{ij}. For particles that come in contact with a wall, the no-slip boundary condition needs to be applied. A proper implementation of this condition is of importance in the scope of current work, as in most cases studied later, the fluid comes in contact with wall at comparably large velocities. The method of Holmes et al. [25] has been implemented here.
SPH particles subjected to negative pressures show tendency of forming small clusters. While simulation results are typically not significantly affected in the larger scale from this arrangement, it becomes important for the test cases of interest here. Having large impact velocities leads to large displacements in particle positions. As the solidification front moves across

the particles, freezing of a portion of particles in a cluster can lead to unstable solutions. The model of Monaghan [26] is used here by adding a correction term to the momentum equation which adjusts particles when negative pressures are present.

2.2 Energy equation

The energy equation here is solved using the methodology proposed by Cao et al. [21]. The three dimensional energy equation for laminar flow with no viscous dissipation is

$$\frac{\partial}{\partial t}(\rho H)+\frac{\partial}{\partial x}(\rho u H)+\frac{\partial}{\partial y}(\rho v H)+\frac{\partial}{\partial z}(\rho w H)=\frac{\partial}{\partial x}\left(k\frac{\partial T}{\partial x}\right)+\frac{\partial}{\partial y}\left(k\frac{\partial T}{\partial y}\right)+\frac{\partial}{\partial z}\left(k\frac{\partial T}{\partial z}\right) \quad (7)$$

For an incompressible fluid,

$$\frac{dH}{dT}=C(T) \quad (8)$$

Enthalpy is calculated with respect to a reference point. In the current context, the reference point is chosen to be the melting point of the solid material. At this temperature, enthalpy is assumed to be zero (see figure 1).

2.2.1 Temperature Calculation

Using this assumption along with equation 8, temperature can be calculated. For a pure substance with phase change at a single temperature,

$$T=\begin{cases} T_m+H/C_s & H\leq 0 \\ T_m & 0<H<L \\ T_m+(H-L)/C_l & H\geq L \end{cases} \quad (9)$$

and for materials like alloys where phase change occurs over a temperature range,

$$T-T_1=\begin{cases} H/C_s & H\leq 0 & solid \\ \Delta T H/(L+C_m\Delta T) & 0<H<L+C_m\Delta T & mushy \\ H/C_l-\left[L+(C_m-C_l)\,\Delta T\right]/C_l & H\geq L+C_m\Delta T & liquid \end{cases} \quad (10)$$

As shown in figure 1, for materials where phase change occurs at a single temperature, enthalpy experiences a step jump at the melting temperature (T_m). For materials such as alloys with a phase change temperature interval (PCTI), phase change occurs over a temperature range T_1 to T_2. When the temperature is within the PCTI, the material is mushy. In the current study and equation 10, enthalpy is assumed to vary linearly over the PCTI.

2.2.2 Kirchhoff temperature

In order to eliminate the constant values in equations 9 and 10, the Kirchhoff temperature is defined as $T^*=\int_{T_{ref}}^{T}k(\zeta)d\zeta$. Applying this definition to equations 9 and 10 gives

$$T^* = \begin{cases} k_s(T - T_m) & T < T_m \\ 0 & T = T_m \\ k_l(T - T_m) & T > T_m \end{cases} \tag{11}$$

for a material with a single phase change temperature and

$$T^* = \begin{cases} k_s(T - T_1) & T \leq T_1 \\ k_m(T - T_1) & T_1 < T < T_2 \\ k_l(T - T_1) & T \geq T_2 \end{cases} \tag{12}$$

for a material that changes phase over a temperature interval.
The constant values T_m and T_1 can now be omitted by substituting T from equations 9 and 10 into equations 11 and 12, respectively. This gives the Kirchhoff temperature as a function of enthalpy in the form of

$$T^* = \begin{cases} k_s H/C_s & H \leq 0 \\ 0 & 0 < H < L \\ k_l(H - L)/C_l & H \geq L \end{cases} \tag{13}$$

for a single phase change temperature and

$$T^* = \begin{cases} k_s H/C_s & H \leq 0 \\ k_m \left[\Delta T H/(L + C_m \Delta T)\right] & 0 < H < L + C_m \Delta T \\ k_l \left[H/C_l - \left[L + (C_m - C_l)\Delta T\right]/C_l\right] & H \geq L + C_m \Delta T \end{cases} \tag{14}$$

for phase change over a temperature range. The linearity of equations 13 and 14 allows the calculation of H or T^* when only one is known.

2.2.3 Source terms

Expressing $T^* = \Gamma(H)H + S(H)$, Γ and S can be derived from equations 13 and 14 as

$$\Gamma(H) = \begin{cases} k_s/C_s & H \leq 0 \\ 0 & 0 < H < L \\ k_l/C_l & H \geq L \end{cases} \quad S(H) = \begin{cases} 0 & H \leq 0 \\ 0 & 0 < H < L \\ -Lk_l/C_l & H \geq L \end{cases} \tag{15}$$

for a single temperature phase change and

$$\Gamma(H) = \begin{cases} k_s/C_s & H \leq 0 \\ k_m \Delta T/(L + C_m \Delta T) & 0 < H < L + C_m \Delta T \\ k_l/C_l & H \geq L + C_m \Delta T \end{cases}$$

$$S(H) = \begin{cases} 0 & H \leq 0 \\ 0 & 0 < H < L + C_m \Delta T \\ k_l \left[L + (C_m - C_l)\Delta T\right]/C_l & H \geq L + C_m \Delta T \end{cases} \tag{16}$$

for phase change over a temperature range.

2.2.4 Reconstruction of Lagrangian energy equation

With the definition of T^*, equation 7 can be rewritten as

$$\frac{\partial}{\partial t}(\rho H) + \frac{\partial}{\partial x}(\rho u H) + \frac{\partial}{\partial y}(\rho v H) + \frac{\partial}{\partial z}(\rho w H) = \frac{\partial^2 T^*}{\partial x^2} + \frac{\partial^2 T^*}{\partial y^2} + \frac{\partial^2 T^*}{\partial z^2} \tag{17}$$

and further expansion of T^* using equations 15 or 16 transforms equation 17 into

$$\frac{\partial}{\partial t}(\rho H) + \frac{\partial}{\partial x}(\rho u H) + \frac{\partial}{\partial y}(\rho v H) + \frac{\partial}{\partial z}(\rho w H) = \frac{\partial^2 (\Gamma H)}{\partial x^2} + \frac{\partial^2 (\Gamma H)}{\partial y^2} + \frac{\partial^2 (\Gamma H)}{\partial z^2} + \frac{\partial^2 S}{\partial x^2} + \frac{\partial^2 S}{\partial y^2} + \frac{\partial^2 S}{\partial z^2} \tag{18}$$

For simplicity of notations, equation 17 can be rewritten as

$$\frac{\partial}{\partial t}(\rho H) + \boldsymbol{\nabla}.(\rho H \boldsymbol{V}) = \nabla^2 T^* \tag{19}$$

By expanding $\boldsymbol{\nabla}.(\rho H \boldsymbol{V})$ into

$$\frac{\partial}{\partial t}(\rho H) + \boldsymbol{V}.\boldsymbol{\nabla}(\rho H) + (\rho H)\boldsymbol{\nabla}.\boldsymbol{V} = \nabla^2 T^* \tag{20}$$

the first two terms on the left hand side can be combined to form a total derivative,

$$\frac{D(\rho H)}{Dt} = -(\rho H)\boldsymbol{\nabla}.\boldsymbol{V} + \nabla^2 T^* \tag{21}$$

Equation 21 for the total derivative is the Lagrangian form of the transformed enthalpy equation. This equation gives the variation of ρH with time for each SPH particle. Using the Lagrangian continuity equation $\frac{D\rho}{Dt} + \rho \boldsymbol{\nabla} \cdot \boldsymbol{V} = 0$, the term $-\rho \boldsymbol{\nabla} \cdot \boldsymbol{V}$ in equation 21 can be replaced by the total derivative of density resulting in

$$\frac{D(\rho H)}{Dt} = H\frac{D\rho}{Dt} + \nabla^2 T^* \tag{22}$$

2.3 SPH discretization

The enthalpy equation, in the form of equation 22, is discretized using an SPH formulation here. This equation resolves enthalpy while applying the effects of phase change latent heat. Here, ρH is taken as a single variable. At each iteration, the variation of ρH with respect to time is calculated and is used to obtain a new value for ρH for each particle in an explicit manner. Wherever a value of H is needed, ρH for that particle is divided by its density. In this case, equation 22 for particle i is written as

$$\frac{D(\rho H)_i}{Dt} = H_i\frac{D\rho_i}{Dt} + (\nabla^2 T^*)_i = H_i\frac{D\rho_i}{Dt} + (\nabla^2 \Gamma H)_i + (\nabla^2 S)_i \tag{23}$$

In equation 23, the values for H_i and $D\rho_i/Dt$ are known for each particle. The Laplacians for ΓH and S must be discretized and calculated in SPH form. Following classic SPH formulations, these Laplacians can be broken into two steps in the form of

$$(\nabla^2 \Gamma H)_i + (\nabla^2 S)_i = \boldsymbol{\nabla_i} \cdot (\boldsymbol{\nabla_i}(\Gamma H) + \boldsymbol{\nabla_i} S) \tag{24}$$

The inner gradient can be calculated here using

$$\boldsymbol{\nabla} f(x_i) = \sum_j^N \frac{m_j}{\rho_i} \left[f(x_j) - f(x_i) \right] . \boldsymbol{\nabla_i} W_{ij} \tag{25}$$

while the outer divergence is calculated from

$$\boldsymbol{\nabla . \Phi(x_i)} = \rho_i \left[\sum_j^N m_j \left(\frac{\boldsymbol{\Phi(x_i)}}{\rho_i^2} + \frac{\boldsymbol{\Phi(x_j)}}{\rho_j^2} \right) . \boldsymbol{\nabla_i} W_{ij} \right] \tag{26}$$

In this manner, the inner gradient in equation 23 becomes

$$\boldsymbol{G_i} = \boldsymbol{\nabla_i}(\Gamma H) + \boldsymbol{\nabla_i} S = \sum_j^N \frac{m_j}{\rho_i} \left\{ [\Gamma(H_j) H_j + S(H_j)] - [\Gamma(H_i) H_i + S(H_i)] \right\} \boldsymbol{\nabla_i W_{ij}} \tag{27}$$

Here, the values for Γ and S are calculated using equations 15 and 16 using the values of H at the particles i and j. Then the outer divergence in equation 24 becomes

$$(\boldsymbol{\nabla . G})_i = \rho_i \left[\sum_j^N m_j \left(\frac{\boldsymbol{G_i}}{\rho_i^2} + \frac{\boldsymbol{G_j}}{\rho_j^2} \right) . \boldsymbol{\nabla_i W_{ij}} \right] \tag{28}$$

These classic SPH discretizations may become unstable when there is a discontinuity in the physical properties in the domain [27], for example, heat transfer between two materials with different thermal conductivities. To overcome this issue, the remedy of Cleary et al. [27] is extended and applied here. In this manner, the Laplacians in equation 23 are directly calculated using

$$\nabla^2 (\Gamma H + S)_i = \sum_j^N 2 \frac{m_j}{\rho_j} (f_i - f_j) \frac{\boldsymbol{\nabla_i} W_{ij}}{\boldsymbol{r_{ij}}} \tag{29}$$

where the variable f is defined as

$$\begin{aligned} f_i &= \Gamma_{eff} H_i + S_i \\ f_j &= \Gamma_{eff} H_j + S_j \end{aligned} \tag{30}$$

and Γ_{eff} is defined as

$$\Gamma_{eff} = \begin{cases} \frac{2\Gamma_i \Gamma_j}{\Gamma_i + \Gamma_j} & \Gamma \neq 0 \\ 0 & otherwise \end{cases} \tag{31}$$

Substituting back into equation 23, the variations of ρH for particle i is calculated from

$$\frac{D(\rho H)_i}{Dt} = H_i \left(\frac{D\rho}{Dt} \right)_i + \nabla^2 (\Gamma H + S)_i \tag{32}$$

2.4 Mushy region treatment

As discussed before for the case of alloys, phase change goes through a mushy zone during melting and solidification. The existence of this region is due to the difference in phase change temperatures of elements forming the alloy. One element might start the solidification process sooner and along the way, the solid crystals that will nucleate and grow will lead to a slurry of solid and molten materials. This phenomena might happen in various ways. In one, the solidified phases might be growing at discrete sites. In this manner, the physical properties of the mixture will be closer to those of a suspension of solid phases in a liquid phase. On the other hand, the solidification might be happening as a solid front growing from a wall. This solid front will have smaller scale porous branches that spread into the heart of the still molten phase. In this manner, the liquid phase will be flowing through the porous solid phase that is growing in size. The flow in this case will be close to flow of liquid phase through porous material. Detailed explanations of these conditions can be found in the work of Voller et al. [28].

The effect of the mushy region is typically included in one of two ways. When the flow pattern is similar to flow through porous media, a Darcy source term can be added to the momentum equation, to account for the pressure drop for the fluid moving through pores. This flow is usually found in casting problems [28]. When the flow is more homogeneous, the effect of having a slurry-like mixture is accounted for by modifying the viscosity. In the current study, this approach has been chosen as it avoids variations in pressure forces that can lead to instabilities in SPH. Depending on the temperature or enthalpy values, a liquid fraction α and a solid fraction $\beta = 1 - \alpha$ can be defined for each particle at each iteration. Based on these values, the viscosity of each particle is updated using [28]

$$\mu = \alpha \ \mu_{liquid} + \beta \ \mu_{solid} \tag{33}$$

For particles that have a liquid fraction of unity, a new viscosity will be equal to the viscosity of the molten material. For liquid fractions of zero, the viscosity of each particle is set to very large to mimic solid matter. In between these two limits, viscosity is varied linearly. Some researchers have substituted this linear variation with [29]

$$\mu = \mu_{liquid} \left(1 + C \frac{\beta^3}{(1-\beta)^3 + \epsilon} \right) \tag{34}$$

where C is a problem dependent constant and ϵ is introduced to avoid division by zero. The values for viscosity need to be calibrated for different materials and conditions. As will be shown later, equation 33 provides more stable solutions in the current framework and hence has been utilized in this study.

3 Validation and Results

3.1 Conduction Problem

3.1.1 Comparison to Analytical Solution

Similar to Cleary et al. [27], a two-dimensional infinite slab is assumed in $x - y$ plane with a temperature discontinuity in its middle at $x = 0$. The material properties are ρ_1, k_1, C_1

when $x < 0$ and ρ_2, k_2, C_2 when $x > 0$. The transient analytical solution to this problem with an initial temperature jump of T_0 across the discontinuity is in the form of [30]

$$T - T_{01} = \begin{cases} \frac{k_1\alpha_1^{-1/2}T_0}{k_1\alpha_1^{-1/2}+k_2\alpha_2^{-1/2}} \left[1 + \frac{k_2\alpha_2^{-1/2}}{k_1\alpha_1^{-1/2}} erf\left(\frac{x}{2\sqrt{\alpha_1 t}}\right)\right] & x > 0 \\ \frac{k_1\alpha_1^{-1/2}T_0}{k_1\alpha_1^{-1/2}+k_2\alpha_2^{-1/2}} \left[erfc\left(\frac{|x|}{2\sqrt{\alpha_2 t}}\right)\right] & x < 0 \end{cases} \tag{35}$$

Here, $\alpha = k/\rho C$ is the thermal diffusivity. To avoid the complications of modeling an infinite slab, the problem is modeled here with slight modifications[27]. To make the heat transfer one dimensional, a periodic boundary condition is applied perpendicular to heat flow direction in y direction. The x axis is also limited to $-1 < x < 1$ and a no-heat flux boundary condition is applied to it ends. It is evident the temperature profile will be slightly different than the analytical solution near the x limits, especially as time goes to infinity. The value of the temperature across all points should converge to $T_0/2$ by the end. These test cases are conducted with 80 particles in x direction. For the first case, the temperature jump and all thermal properties are taken to be unity. Figure 2 shows the temperature profile for this case for 0, 1, 3, 8, 10, and 20μs. The solid lines in this figure are the analytical solutions obtained from equation 35. As expected, temperature values near the x limits of -1 and 1 start deviating from the analytical solution as time becomes larger. The values of temperature in the middle of the slab however are a good match to the analytical solution. The second case shows performance under discontinuity in thermal properties. The temperature jump is taken to be 10 and thermal properties of materials are same as before with the exception of $k_1 = 10$.
Figure 3a clearly shows that for small times, the simulation produces a perfect match to the analytical solution. As time grows, so does the error especially close to the boundaries. The error values for this test case, calculated in the form of $L_2 = \sqrt{\frac{1}{N}\sum_{i=1}^{N}(T_i^{SPH} - T_i^{exact})^2}$, are plotted in figure 3b.

3.1.2 Comparison to Numerical Solution

For numerical comparison, result generated by the ANSYS Fluent software (Canonsburg, PA, USA) is used as benchmark. A two-dimensional solid square plate with a dimensionless side length of 1 is considered. The transient heat conduction inside this square is captured as it is heated from its sides. For simplicity, the density, thermal conductivity, and heat capacity are all chosen to be unity as well. The plate is initially at zero temperature. At $t > 0$, the temperature of the walls is set to unity. The test case is performed once using the SPH solver presented here, and once using the Fluent solver. Transient temperature profile on the diagonal of the square and the error values have been plotted in figures 4a and 4b, respectively.

3.2 Two-dimensional Problem: Phase Change in the Corner of a Square

For the test cases described below, SPH particles are uniformly distributed with spacing of $\Delta x = \Delta y$ over the cross section of the cuboid as shown in figure 5a. Domain is periodic

in z direction. Since each particle has a neighbourhood with a radius of $3\Delta x$, 3 layers of particles have been placed in the wall in order to make sure all inner particles have a complete neighbourhood. Depending how the values of gradients at wall particles are calculated, these 3 layers of particles might need to have a full neighbourhood of particles. Although test cases show results are not much affected by this, in order to have valid gradients calculated at these 3 layers of wall particles, an extra 3 more layers are also added in the walls here to make sure all wall particles that directly interact with inner particles have a full neighbourhood. The value of temperature of all wall particles are kept constant through all iterations.

3.2.1 Comparison to Numerical Results

The numerical results available in literature for the Stefan problem are used for numerical validation of the model in the presence of phase change. To simulate the Stefan problem, the three dimensional cuboid shown in figure 5b is filled with fluid which is at liquid state initially. Solidification will start as the temperature of the walls drop to a value below freezing. This problem has been widely used in literature as a benchmark. In most of reported cases, only a portion of cuboid cross section is simulated (1/4 or 1/8). The boundaries inside fluid for these cases are assumed adiabatic due to the symmetry in this problem. Here however the prism is fully modelled. In z direction, a periodic boundary condition is imposed. For the wall, as SPH particles here see three particles immediate to them in their neighbourhood based on current configurations, three layers of particles with static ρH values are placed on the wall. In this way, it is made sure that all inner particles have complete wall neighbouring particles with wall temperature. All properties for solid and liquid are assumed to remain constant in each phase. Density is also assumed to be constant and equal for both phases.
For the initial problem, fluid is assumed to be in liquid form and close to freezing temperature. Wall temperature is suddenly dropped below freezing point and solidification starts from the boundaries toward the centre of cuboid. Fluid and solid properties are assumed to be constant and the values for non-dimensional parameters are $\theta = (T_i - T_w)/(T_m - T_w) = 1$ and $St = C_s(T_m - T_w)/L = 0.641$. Figure 6a shows the solidification front along the diagonal of cross section of the cuboid. For comparison, results reported by Cao et al. [21], Crowley [31], and Hsiao et al. [12] have also been plotted in this figure.
The second problem has the same configuration as before with only the initial temperature being at a value larger than phase change temperature. Non-dimensional parameters for this problem are $\Theta = (T_i - T_w)/(T_m - T_w) = 9/7$ and $St = C_s(T_m - T_w)/L = 2$, $\alpha_l/\alpha_s = 0.9$, and $k_l/k_s = 0.9$. Figure 6b compares results for this test case against results of Cao et al. [21], Hsiao et al. [12], and Keung [32].

3.2.2 Effect of ΔT

The same test case has also been conducted using the same properties and the assumption that phase change occurs at a temperature range of $\Delta T = 20$. As evident, results shown in figure 6b are not sensitive to allowing the phase change to occur over a temperature range.

3.2.3 Effect of particle resolution

To make sure solution is not dependent to the initial particle positioning (particle resolution), different resolutions has been chosen for problems above. Figure 7a shows variation of results as resolution is changed from 10×10 to 100×100. It can be seen that by increasing the resolution, results converge to unique values. Results remain nearly identical for resolutions above these values.

3.2.4 Effect of Smoothing Kernel

Effect of choosing different smoothing functions has also been studied by choosing four common smoothing functions shown in table 1. First example from before has been repeated using each of these kernels. Figure 7b shows that the choice of smoothing kernel will not affect final results.

3.3 Three-dimensional Problem: Droplet Impact & Solidification

The three-dimensional problem of interest here is impact and solidification of a molten drop. For comparison, test case conditions are chosen similar to test case of Aziz et al. [33] and Pasandideh et al. [34]. In this problem, a molten tin drop is impacted on a stainless steel substrate. The drop is initially at 240°C. The substrate is at room temperature. The impact is occurring at a low velocity of 1m/s. The drop has an initial diameter of $2.7mm$. The spread factor (D/D_0) for this test case has been plotted in figure 8. Experimental results of Aziz et al. [33], and numerical result of Pasandideh et al. [34] have also been plotted here for comparison. Results indicate a good agreement to other numerical and experimental results for spread factor of the low velocity impacting drop. The final prediction for the spread factor here is closer to the numerical results of Pasandideh et al., both deviating near 6% from Aziz et al. experimental values.

3.4 Mushy zone

Providing an exact benchmark for the mushy implementation methods seems impossible for various reasons. There are not any robust and accurate empirical measurements of the mushy region available to match the framework of this work. For the numerical studies that have been dedicated to this matter, the typical problem that has been studies is natural convection. In this case, the material is allowed to solidify in a cube (or corner in 2D). During this process, the natural convection resulting from temperature variations will accelerate molten liquid to flow similar to a lid-driven cavity problem. This will result in an uneven growth of the solid front and can be used as a tool to measure the capability of mushy region handling. In the implementation in this work, however, the small time steps enforced on the simulation will make modeling of a natural convection cavity problem cumbersome. Therefore, instead a more relaxed problem has been chosen here to provide a qualitative comparison of the formulations. In this problem, solidification problem in a cavity under natural convection is studied. However, in order to avoid long wait times for the flow pattern to form, a divergence free velocity field in the form of $v_\theta = 20\frac{r}{R}$ and $v_r = 0$ is imposed on the fluid at the start of the simulation. Figure 9a shows schematic drawing of this problem. Liquid phase here is

confined inside a cavity. The lower and upper walls are isolated. The fluid is allowed to have heat transfer only with a cold and hot source on each side. The red arrows in this figure show the initial velocity field in the domain.
Particle positions for this test case after the solidification has been partially completed is shown in figure 9c at $t = 0.16$. The solidification front (for $\alpha = 0.5$) for equations 33 and 34 at this time has also been plotted in figure 9b. It becomes evident that though both formulations used here provide similar results, the particle positions and arrangements are better preserved using 33. Hence, equation 33 has been used to capture mushy effects in the current study.

3.5 Application to Suspension Plasma Spraying (SPS)

3.5.1 Spread Factor

As impact points of YSZ particles generated by suspension plasma spraying are well-spread on the substrate, the larger size droplets make the main contribution in creating roughness, by having splats that overlap one another. Smaller size particles mostly create isolated bumps, as the possibility of having direct binary impacts in short time periods is low, and because the spread factor for these smaller droplets is not relatively large.
To get a better prediction on the final conditions of the substrate, the SPH solver has been used here to calculate spread factor at three different velocities of 50, 100, and $200m/s$, which covers the velocity range of YSZ droplets impacting the substrate obtained from SPS simulation. Results of this test case are plotted in figure 10 as a function of the non-dimensional time ($t^* = tV/D_0$). These configurations leads to non-dimensional values of 96, 192, 383 for $Re = \frac{\rho V_0 D_0}{\mu}$, and 323, 1293, 5172 for $We = \frac{\rho V_0^2 D_0}{\sigma}$. Since Weber numbers here are much larger compared to Reynolds values, i.e. $We \gg \sqrt{Re}$, the capillary effects can be neglected [35]. Pasandideh-Fard et al. [35] have predicted that for these conditions and with $We \gg 12$, spread factor can be approximated by $0.5Re^{0.25}$. Results obtained here also suggest a similar correlation for spread factor in the form of ($R^2 = 0.9960$)

$$\xi_{max} = \frac{D_{max}}{D_0} = 0.59\ Re^{0.28} \tag{36}$$

3.5.2 Solidification Time

A test case is conducted here to examine the solidification time and amount of heat transferred from an individual molten YSZ droplet to the substrate. A droplet with diameter of $3\mu m$ impacts the substrate at $3000K$ and velocity of $150m/s$. The substrate is at $600K$. The substrate is chosen from two different materials. The first is YSZ, identical to the material inside the droplets. For the second, thermal conductivity of the substrate is chosen to be $66W/(m \cdot K)$ (similar to Tin), mimicking initial layer of coating where droplets hit a metallic substrate. Figure 11 shows this droplet at various stages of impact and solidification at non-dimensional times of $t^* = 0.5$, 10, 500, 1000, 1400, and 1500 on the YSZ substrate. Solidification starts from lower parts of the splat, and grows faster near the splat edges and in the middle, potentially due to lower thicknesses and longer contact time with the substrate, respectively. The splat fully solidifies here by nearly $t^* = 1500$.

3.5.3 Heat Flux

Figure 12 shows the amount of heat flux at the impact point of the droplet on the substrate with higher thermal conductivity as a function of non-dimensional time. Results show that moments after impact, the heat transfer to the substrate grows suddenly to a very large value. The reason behind this sudden jump is that at the moment of impact, the substrate and droplet are at their highest temperature difference. Moreover, the impact area between these two is at its smallest near the impact time. As the droplet hits the surface and expands, the area underneath grows and distribute the heat transfer underneath the droplet. As the droplet spreads and loses heat, the temperature difference between the substrate and droplet becomes smaller causing a decrease in heat flux values. The high thermal conductivity of the substrate here contributes to a fast formation of a solidified layer next to the boundary. The cooling process of the material in the bulk of splat is still limited by the low thermal conductivity of the YSZ.

3.5.4 Void Formation

A two-dimensional setup has been used here to study the cases where droplet impacts are prone to void formation. For the test cases below, a droplet with a radius of $3\mu m$ is impacted on a surface. The surface geometry is changed going from a flat surface to surfaces with step sizes of 0.12, 0.24, 0.36, $0.54\mu m$. Impact velocity is $150m/s$ for all the cases. Initial temperature of the substrate is $300K$. All figures have been reported at $t = 0.1\mu s$, which is when the spread and recoil of the droplet have already finished and the shape of the splat is not going through any significant changes.
In the first case, the initial temperature for the droplet is $2985K$. This temperature is slightly above solidification point of YSZ. Results for this test have been shown in figure 13a. Since the drops here are close to their melting point, solidification occurs shortly after they come in contact with the substrate. This prevents any significant pore formation near the step dent on the surface. The SPS data suggest that droplets are typically at higher temperatures above the melting point of YSZ at the time of impact. Hence, the same test case is repeated here with now an initial temperature of $3500K$ for the droplets. Results for this case have been shown in figure 13b. In these cases, as the droplet needs more time to solidify, the spread and recoil occurs while the droplet has not lost enough heat for solidification. The impact this time is being controlled by the momentum force spreading the drop over the step boundary and surface tension forces acting upon it. Here the pore that is formed is nearly a quarter of circle whose radius is very close to the the step height. A possible explanation for this behavior might be due to large surface tension magnitude of molten YSZ, which forces the splat to form a nice curvature over the discontinuity. It is evident where the temperature was close to melting point of YSZ, the solidification process has prevented pore formation.

3.5.5 Binary Impacts

Another case of importance comes from examination of YSZ droplets obtained from SPS data. Results indicate that many of the binary impacts of splats occurring on the substrate involve $4 - 6\mu m$ droplets. This is due to the fact that these droplets are large enough to create big splats that can effectively contribute to overlaps and surface coverage. In this

manner, a test is performed here for impact of a candidate droplet from SPS data with a diameter of $4.59\mu m$ impacting the substrate at $175m/s$ with a temperature of $3517K$. The solidified splat for this case is shown in figure 14a. The impact and spread of this drop on the substrate is finished by nearly $t^* = 110$. It then takes up to $t^* = 1500$ for the splat to fully solidify.
From the binary impacts involving the droplet shown in figure 14a, a common sample is chosen as an example here, where the splat generated by the droplet mentioned before with diameter of $4.59\mu m$ is impacted by a droplet with diameter of $6.8\mu m$ at a velocity of $231m/s$ and temperature of $3795K$. The point of impact for this droplet is nearly $14\mu m$ away from the center of impact of the first droplet. Result of this binary impact is shown in figure 14b. As the time between the two impacts is much longer than the solidification time, it is safe to assume that the first droplet's splat has already solidified by the time the second droplet impacts. It can be observed that the second droplet becomes more spread in the free directions where there were no obstacles, in contrast to the direction where the splat from first droplet is present. In that direction, the second splat has spread into three main branches, two bypassing the first droplet's solidified splat, and one being forced to splash over it.

3.5.6 Multiple Impacts

Analyzing impact points of the SPS data reveals that only a handful will have close impact points on the substrate in short time intervals. This comes from high efficiency of the SPS process in coating the surface, as the mist of droplets generated from atomization of liquid suspension uniformly covers a large area, making it impossible to get multiple impacts on a particular place of the substrate in a short time interval. As an starting point, a site on the substrate has been chosen for further study, where SPS data shows close impact of 5 droplets. Although not all of these 5 droplets have direct impacts, they will eventually overlap when their splats spread over the substrate. location and properties of these droplets at the time of impact are provided in table 2. As evident, droplets in this neighborhood cover a wide range of possible diameters that are found during the SPS coating process.
Velocity components parallel to the substrate, though small in magnitude, have also been included in this simulation. Sample simulation cases show that the impact, spread and solidification of each droplet happens orders of magnitude faster than the impact of the next droplet. Hence, it is reasonable to assume that each droplet is completely solidified before the next droplet impacts close to it. For the simulations here, the material for the droplets and substrate is YSZ. Though at the start of the coating process, the substrate material will play an important role as typical metallic substrates will have higher thermal conductivities compared to YSZ, with more YSZ layers coating the surface over time, the new droplets will mostly impact a substrate covered by YSZ. The droplets are in molten liquid states corresponding to their values in table 2. The contact angle between drops and the surface is taken to be 90° [36], though as it will be discussed later, the capillary effects are negligible since $We \gg \sqrt{Re}$ here [35]. The solidification of molten drops is resolved using equation 22. The mushy zone effects are also included using equation 33. Gravity force is added with a value of $9.81m/s^2$ exerted on molten droplets in the opposite direction of the z axis, although its effect is also not significant.

Results of this case are presented in figures 15-16. Figures have been colored by z magnitude at each point, identifying how the roughness of the substrate changes due to the increase in local height. The first two droplets have larger diameters near $9\mu m$ with impact velocities higher than $200m/s$. Hence, they have large spread factors and the splats cover a large area. The next two drops have smaller diameters near $3\mu m$ and lower impact velocities below $100m/s$. The last drop also has a small diameter, but impacts at the highest speed. The final coated substrate after five impacts is plotted in figure 16. The maximum height from substrate's surface for each solidified droplet is 0.91, 1.76, 1.53, 2.40, and 2.14 μm, for droplets #1 to #5, respectively. Hence, the highest peak in the finished coating corresponds to a height of $2.40\mu m$, which is achieved from overlapping splats of droplets #1, #2, and #4.

3.5.7 Predictions for Finished Coating

Using the information gathered, a Matlab routine is used to apply the generated information to a larger portion of the collected SPS data. Direct simulation of these impacts using SPH is computationally expensive. SPS data used here contains a total of one million SPS droplet impacts gathered on the substrate sprayed over $0.61s$.
In the Matlab routine, equation 36 has been used for predicting the spread diameter of SPS droplets on the substrate. It has been assumed that solidified splats are in the form of discs on the substrate. The tangential component of the impact velocities has been neglected. Results of simulations in previous sections suggested that when a droplet at high temperature impacts an uneven surface, there is a high chance for void formation with a similar size to the height of the void. This has also been included here by making the assumption that droplets impacting the surface with high temperatures will contribute to formation of voids beneath them, though the dimensions of the voids are small compared to other dimensions. Application of these procedures to the example of five droplets of table 2 is shown in figure 17a. It can be observed that using this method, the overall behavior of impacts can been predicted as the high and low points in both simulation and prediction are close. The routine is now applied to the 1 million droplets. Substrate coating at multiple scales has been shown in figure 17b. Over the $0.61(s)$ spray time, 69.80% of the total solid mass of YSZ initially injected into the domain has been deposited onto the substrate, leading to a deposition efficiency of 69.80%. Growth of the area of the solidified material on the substrate as a function of time for this 1 million droplets has been shown in figure 18.

4 Conclusion

Modeling heat transfer with phase change in SPH has been investigated by study of impact and solidification of ceramic droplets on the surface. Release and absorption of latent heat during phase change is accounted for by non-linear transformation of enthalpy equation by adding source terms. This model has been validated against various available analytical, experimental, and numerical results from literature. Results indicate that the enthalpy formulation provides a reliable platform for capturing phase change in free surface flows. It also provides the opportunity of modeling pure materials without the need of introducing a

phase change interval.
The new formulation has been applied to substrate coating process in Suspension Plasma Spraying (SPS). Combining data of YSZ droplets collected on a substrate with the splat formation and solidification results obtained from SPH solution shows that the surface is coated by isolated splats solidifications. Impacted droplets complete their impact and recoil cycle by $t^*(= tv/D)$ values below 10. t^* has to grow to $1000 - 1500$ for the splat to fully cool down and solidify due to the high temperature of molten ceramics at impact.
As the SPS data indicates a wait time of $t^* = 300,000$ to 5 million between successive impacts, it has been concluded that it is rare for two droplets to hit one another on the substrate while both in molten state. Findings also suggest noticeable differences between the first coating layer compared to others. For YSZ droplets that come in direct contact with metallic substrates, higher thermal conductivity of the substrate material will contribute to fast formation of a solid layer beneath the splat that will eventually immobilize it. For next layers of coating, where YSZ droplets hit solidified YSZ splats, lower thermal conductivities results in a delayed cooling, allowing better spread of droplets on the substrate.

References

[1] AJ Dalhuijsen and A Segal. Comparison of finite element techniques for solidification problems. *International Journal For Numerical Methods in Engineering*, 23(10):1807–1829, 1986.

[2] Philip Li-Fan Liu, Harry Hsiu-Jen Yeh, and Costas Synolakis, editors. *Advanced Numerical Models for Simulating Tsunami Waves and Runup*. World Scientific, 2008.

[3] Bruce Cartwright, PHL Groenenboom, and Damian McGuckin. Examples of ship motion and wash predictions by Smoothed Particle Hydrodynamics (SPH). In *9th Symposium on Practical Design of Ships and Other Floating Structures, Luebeck-Travemuende, Germany*, 2004.

[4] Amirsaman Farrokhpanah and Javad Mostaghimi. Application of multiphase particle methods in atomization and breakup regimes of liquid jets. In *ASME 2014 4th Joint US-European Fluids Engineering Division Summer Meeting*, page V01AT05A009. American Society of Mechanical Engineers, 2014.

[5] Amirsaman Farrokhpanah, Babak Samareh, and Javad Mostaghimi. Droplet impact: A GPU based Smoothed Particle Hydrodynamics (SPH) approach. In *ASME 2012 Fluids Engineering Division Summer Meeting*, pages 615–623. American Society of Mechanical Engineers, 2012.

[6] XY Hu and NA Adams. A multi-phase SPH method for macroscopic and mesoscopic flows. *Journal of Computational Physics*, 213(2):844–861, 2006.

[7] N Grenier, DL Touze, M Antuono, and A Colagrossi. An improved SPH method for multi-phase simulations. In *8th International Conference on Hydrodynamics, ICHD*, 2008.

[8] Alexandre M Tartakovsky, Kim F Ferris, and Paul Meakin. Lagrangian particle model for multiphase flows. *Computer Physics Communications*, 180(10):1874–1881, 2009.

[9] Mohammad Passandideh Fard. Droplet impact and solidification in a thermal spray process: Droplet-substrate interactions. In *Proceedings of the 9th National Thermal Spray Conference*, 1996.

[10] Vaughan R Voller and C Prakash. A fixed grid numerical modelling methodology for convection-diffusion mushy region phase-change problems. *International Journal of Heat and Mass Transfer*, 30(8):1709–1719, 1987.

[11] BG Thomas, IV Samarasekera, and JK Brimacombe. Comparison of numerical modeling techniques for complex, two-dimensional, transient heat-conduction problems. *Metallurgical Transactions B*, 15(2):307–318, 1984.

[12] JS Hsiao and Benjamin TF Chung. An efficient algorithm for finite element solution to two-dimensional heat transfer with melting and freezing. *Journal of Heat Transfer*, 108(2):462–464, 1986.

[13] Amirsaman Farrokhpanah, Markus Bussmann, and Javad Mostaghimi. A new smoothed particle hydrodynamics (sph) formulation for modelling heat conduction with solidification and melting. *arXiv preprint arXiv:1608.04400*, 2016.

[14] PW Cleary, Joseph Ha, John Mooney, and Vikas Ahuja. Effect of heat transfer and solidification on high pressure die casting. In *Proc. 13th Australasian Fluid Mechanics Conference, Melbourne*, pages 679–682, 1998.

[15] P.W. Cleary, J. Ha, M. Prakash, and T. Nguyen. 3D SPH flow predictions and validation for high pressure die casting of automotive components. *Applied Mathematical Modelling*, 30(11):1406–1427, 2006.

[16] Paul W. Cleary. Extension of SPH to predict feeding, freezing and defect creation in low pressure die casting. *Applied Mathematical Modelling*, 34(11):3189–3201, 2010.

[17] Mingyu Zhang, Hui Zhang, and Lili Zheng. Application of Smoothed Particle Hydrodynamics method to free surface and solidification problems. *Numerical Heat Transfer, Part A: Applications*, 52(4):299–314, 2007.

[18] MY Zhang, H Zhang, and LL Zheng. Simulation of droplet spreading, splashing and solidification using Smoothed Particle Hydrodynamics method. *International Journal of Heat and Mass Transfer*, 51(13):3410–3419, 2008.

[19] Mingyu Zhang, Hui Zhang, and Lili Zheng. Numerical investigation of substrate melting and deformation during thermal spray coating by SPH method. *Plasma Chemistry and Plasma Processing*, 29(1):55–68, 2009.

[20] Joseph J Monaghan, Herbert E Huppert, and M Grae Worster. Solidification using Smoothed Particle Hydrodynamics. *Journal of Computational Physics*, 206(2):684–705, 2005.

[21] Yiding Cao, Amir Faghri, and Won Soon Chang. A numerical analysis of Stefan problems for generalized multi-dimensional phase-change structures using the enthalpy transforming model. *International Journal of Heat and Mass Transfer*, 32(7):1289–1298, 1989.

[22] Amirsaman Farrokhpanah, Thomas W Coyle, and Javad Mostaghimi. *Journal of Thermal Spray Technology*, 26(1):12–36, 2017.

[23] J J Monaghan. Smoothed Particle Hydrodynamics and its diverse applications. *Annual Review of Fluid Mechanics*, 44:323–346, 2012.

[24] Alexandre M Tartakovsky and Paul Meakin. A Smoothed Particle Hydrodynamics model for miscible flow in three-dimensional fractures and the two-dimensional Rayleigh–Taylor instability. *Journal of Computational Physics*, 207(2):610–624, 2005.

[25] David W Holmes, John R Williams, and Peter Tilke. Smooth Particle Hydrodynamics simulations of low Reynolds number flows through porous media. *International Journal for Numerical and Analytical Methods in Geomechanics*, 35(4):419–437, 2011.

[26] Joseph J Monaghan. SPH without a tensile instability. *Journal of Computational Physics*, 159(2):290–311, 2000.

[27] Paul W Cleary and Joseph J Monaghan. Conduction modelling using Smoothed Particle Hydrodynamics. *Journal of Computational Physics*, 148(1):227–264, 1999.

[28] VR Voller, AD Brent, and C Prakash. Modelling the mushy region in a binary alloy. *Applied Mathematical Modelling*, 14(6):320–326, 1990.

[29] S Alavi, M Passandideh-Fard, and J Mostaghimi. Simulation of semi-molten particle impacts including heat transfer and phase change. *Journal of Thermal Spray Technology*, 21(6):1278–1293, 2012.

[30] Horatio Scott Carslaw and John Conrad Jaeger. Conduction of heat in solids. *Oxford: Clarendon Press, 1959, 2nd ed.*, 1959.

[31] AB Crowley. Numerical solution of Stefan problems. *International Journal of Heat and Mass Transfer*, 21(2):215–219, 1978.

[32] Chi-Sing Keung. *The use of sources and sinks in solving two-dimensional heat conduction problems with change of phase in arbitrary domains.* PhD thesis, Columbia University, 1980.

[33] Shiraz D Aziz and Sanjeev Chandra. Impact, recoil and splashing of molten metal droplets. *International Journal of Heat and Mass Transfer*, 43(16):2841–2857, 2000.

[34] M Pasandideh-Fard, S Chandra, and J Mostaghimi. A three-dimensional model of droplet impact and solidification. *International Journal of Heat and Mass Transfer*, 45(11):2229–2242, 2002.

[35] Mohammad Pasandideh Fard, Y. M. Qiao, Sanjeev Chandra, and Javad Mostaghimi. Capillary effects during droplet impact on a solid surface. *Physics of Fluids (1994-Present)*, 8(3):650–659, 1996.

[36] Tommy Che-Ming Wu, Markus Bussmann, and Javad Mostaghimi. The impact of a partially molten YSZ particle. *Journal of Thermal Spray Technology*, 18(5-6):957–964, 2009.

[37] Shuai Meng, Rui Yang, Jian-Song Wu, and Hui Zhang. Simulation of droplet spreading on porous substrates using Smoothed Particle Hydrodynamics. *International Journal of Heat and Mass Transfer*, 77:828–833, 2014.

[38] Gordon R Johnson, Robert A Stryk, and Stephen R Beissel. SPH for high velocity impact computations. *Computer Methods in Applied Mechanics and Engineering*, 139(1):347–373, 1996.

[39] Joseph J Monaghan and John C Lattanzio. A refined particle method for astrophysical problems. *Astronomy and Astrophysics*, 149:135–143, 1985.

[40] Gui-Rong Liu and Moubin B Liu. *Smoothed Particle Hydrodynamics: A Meshfree Particle Method*. World Scientific, 2003.

Table 1: Smoothing kernels used in Enthalpy Formulation test cases

Smoothing Kernels	
Meng et al. [37]	$W(R,h) = \frac{21}{16\pi h^3} \begin{cases} (1-R/2)^4(2R+1) & 0 \leq R \leq 2 \\ 0 & otherwise \end{cases}$
Johnson et al. [38]	$W(R,h) = \frac{5}{4\pi h^3} \begin{cases} (3/16)R^2 - (3/4)R + 3/4 & 0 \leq R \leq 2 \\ 0 & otherwise \end{cases}$
Monaghan et al. [39]	$W(R,h) = \frac{3}{2\pi h^3} \begin{cases} 2/3 - R^2 + R^3/2 & 0 \leq R < 1 \\ (1/6)(2-R)^3 & 1 \leq R < 2 \\ 0 & otherwise \end{cases}$
Liu et al. [40]	$W(R,h) = \frac{1}{4\pi h^3} \begin{cases} (2-R)^3 - 4(1-R)^3 & 0 \leq R \leq 1 \\ (2-R)^3 & 1 < R \leq 2 \\ 0 & otherwise \end{cases}$

Table 2: YSZ particles properties at impact

#	x (μm)	y (μm)	u (m/s)	v (m/s)	w (m/s)	T (K)	D (μm)
1	-6.6	3.0	-4.1	1.5	-207.6	3679.8	9.1
2	1.4	-2.9	-0.2	5.9	-226.1	3833.5	8.7
3	10.8	-9.3	27.7	5.1	-88.5	3523.5	3.0
4	4.7	5.7	15.3	16.1	-99.3	3543.3	2.9
5	-10.3	3.6	-8.1	35.3	-227.8	3638.2	4.2

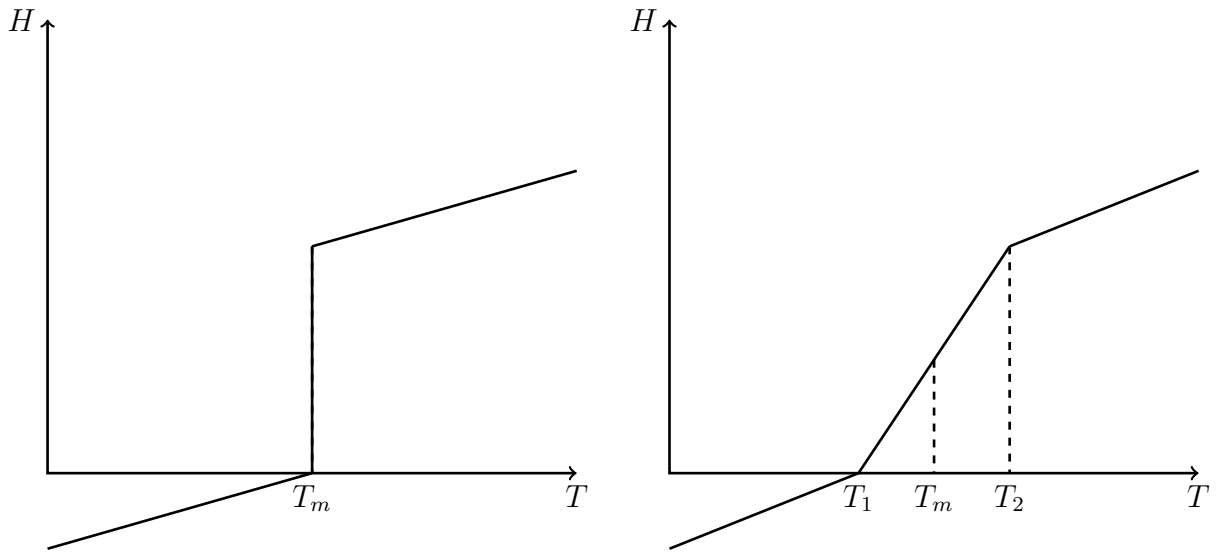

Figure 1: Enthalpy variation for a material with a single phase change temperature (left) and phase change over a temperature interval (right).

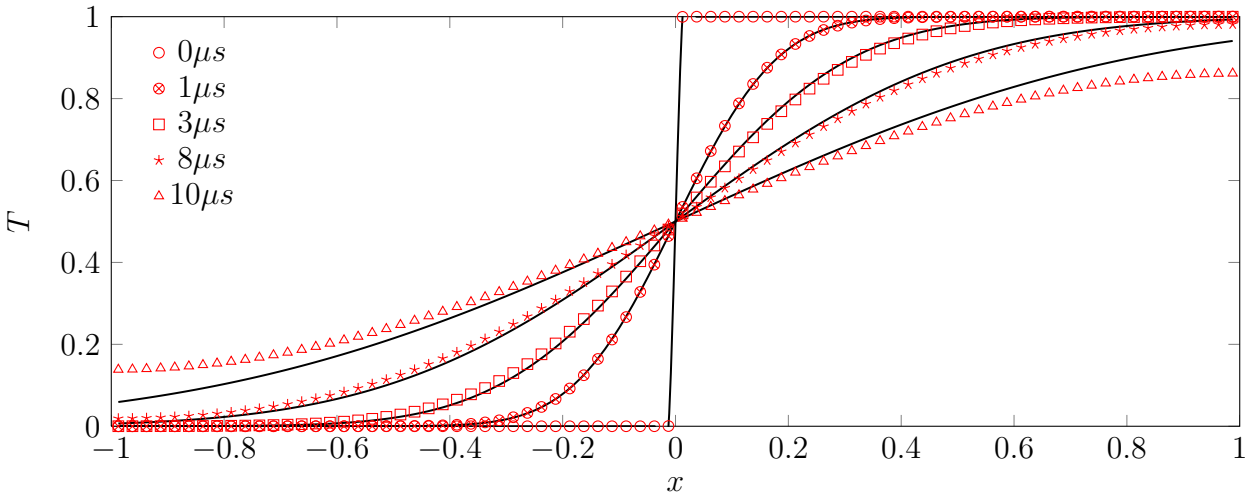

Figure 2: Temperature profile across the slab with an initial unit temperature jump at $x = 0$.

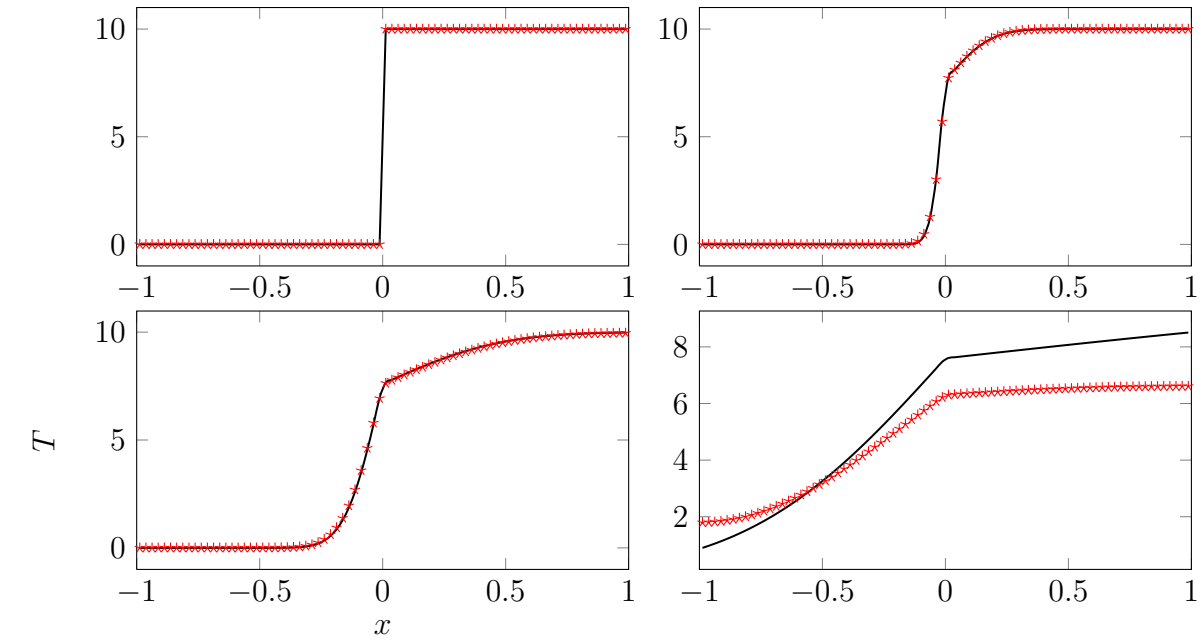

(a) Temperature profile at $t = 0$, $1ms$, $7ms$, and $0.2s$.

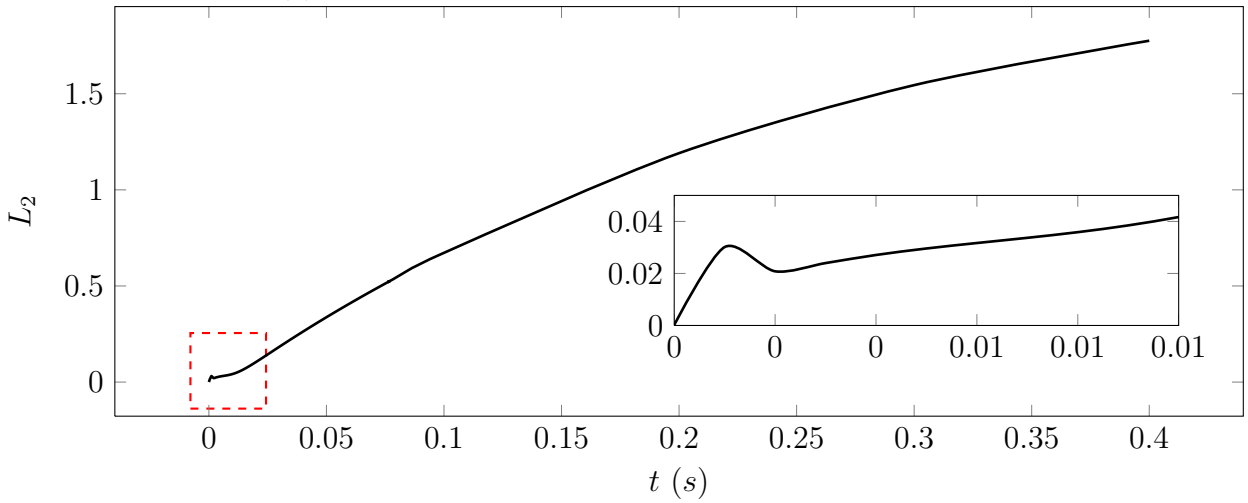

(b) L_2 error values

Figure 3: temperature profile across a slab with a temperature jump of 10.

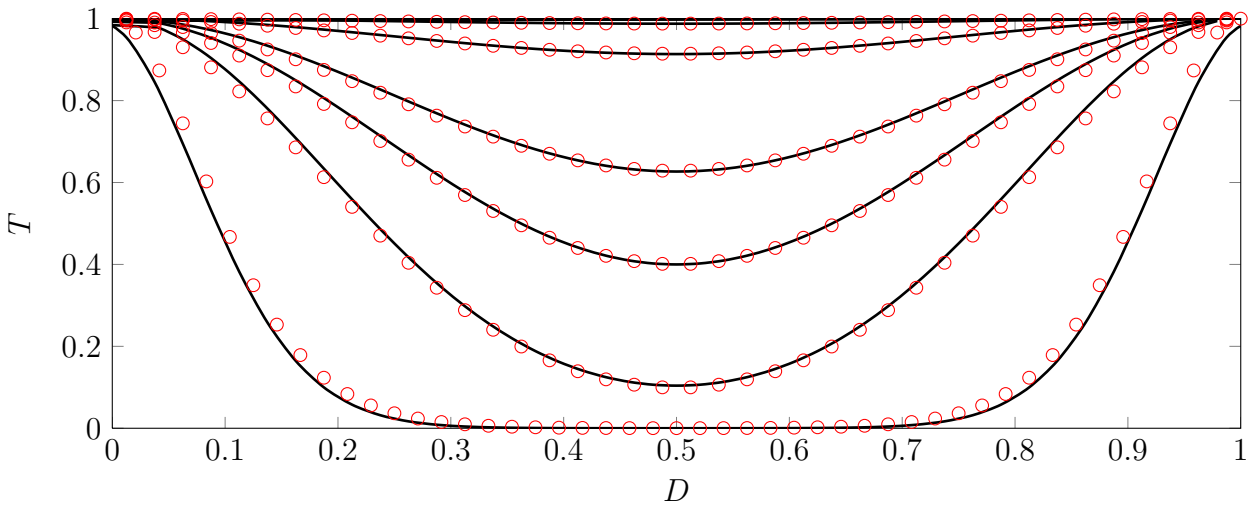

(a) Temperature on the diagonal of the square at $t = 5$, 25, 50, 75, 150, and $250ms$.

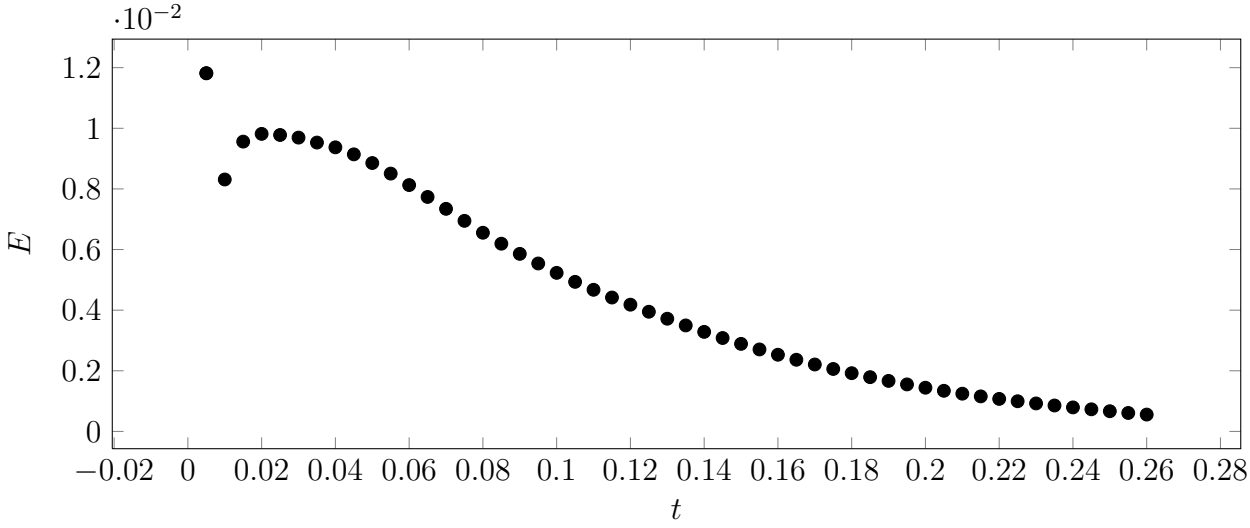

(b) $E = max\left(|T_{SPH} - T_{Fluent}|\right)$

Figure 4: Computed temperature values on the diagonal of the square plate.

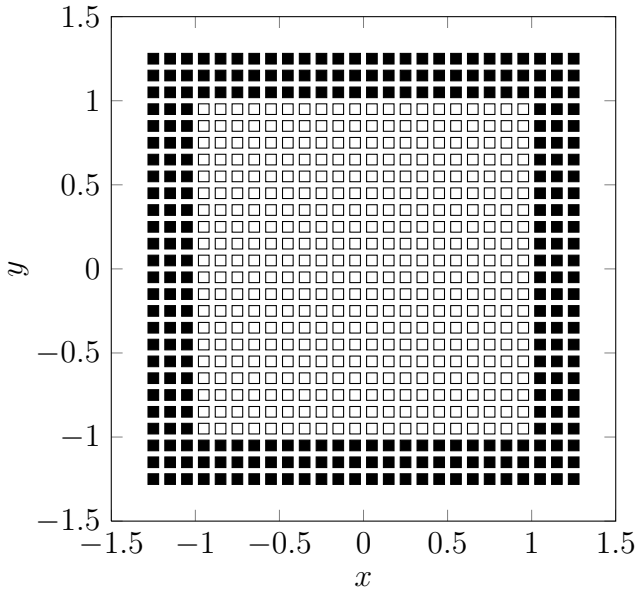

(a) Initial positioning of fluid/solid particles (hollow squares) and wall particles (filled squares)

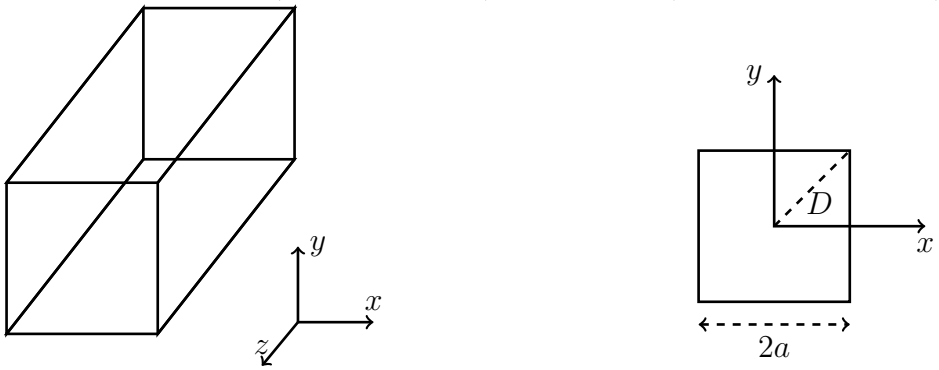

(b) The schematic drawing of the Cuboid which is infinitely long in the z direction.

Figure 5: At the start of simulation, temperature of the walls is dropped to below freezing.

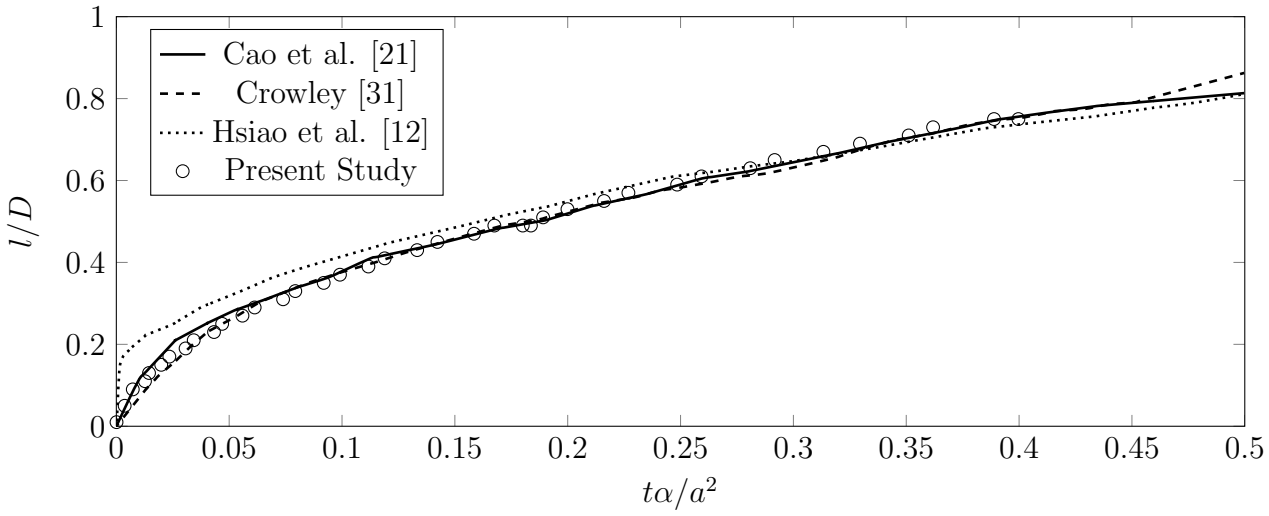

(a) For saturated liquid compared against Cao et al. [21], Crowley [31], and Hsiao et al. [12].

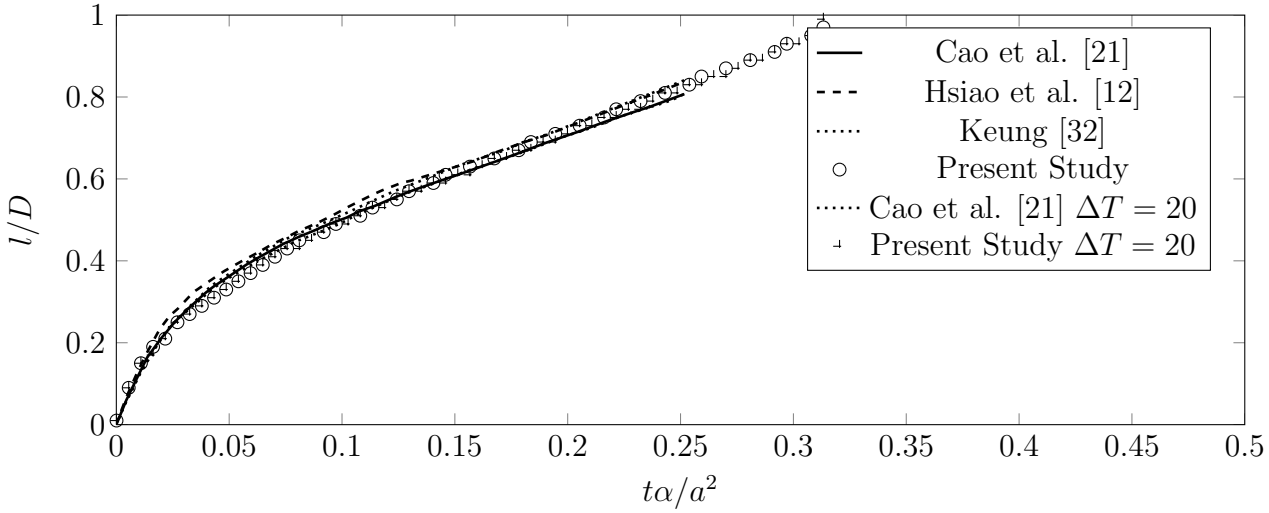

(b) For liquid above freezing temperature compared against Cao et al. [21], Hsiao et al. [12], and Keung [32].

Figure 6: Solidification front moving along the diagonal of a cross section of the cuboid.

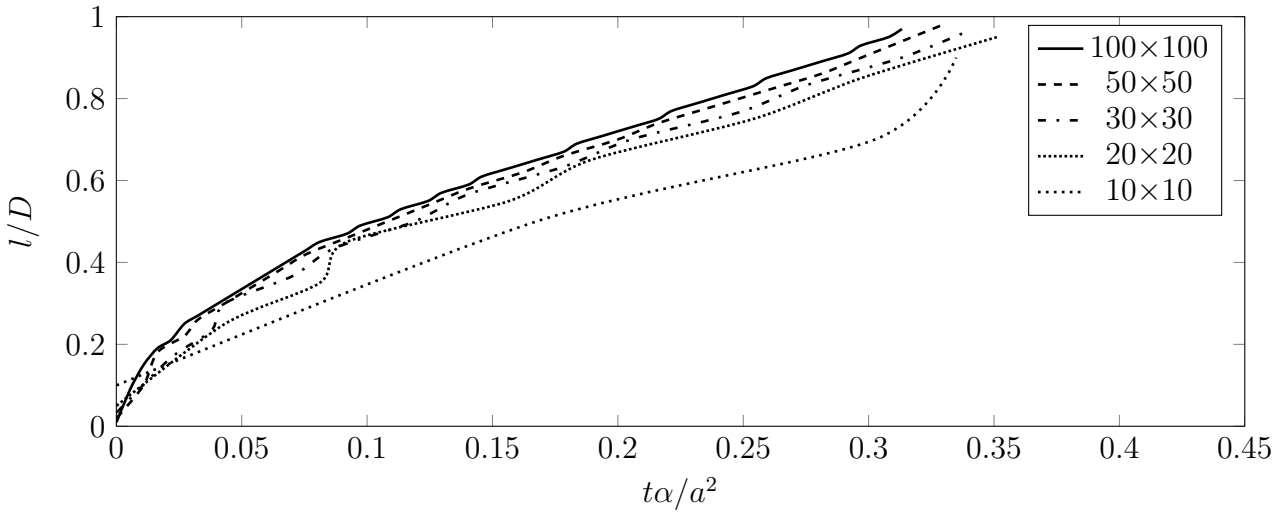

(a) Effect of particle spacing from 10x10 to 100x100 particles.

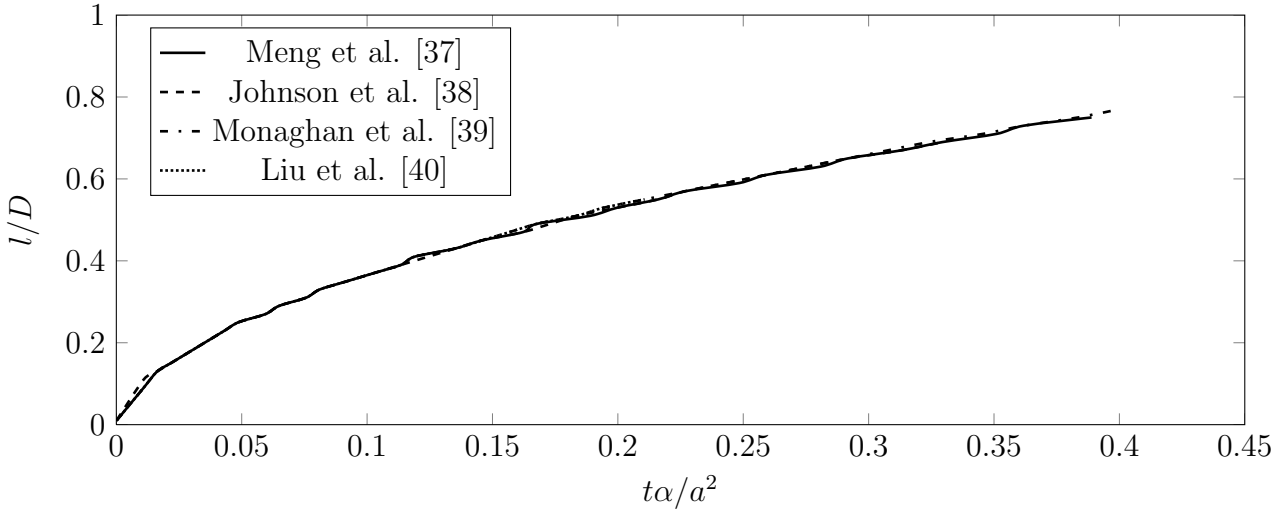

(b) Effect of using different kernels.

Figure 7: Solidification front moving along the diagonal of a cross section of the cuboid for saturated liquid.

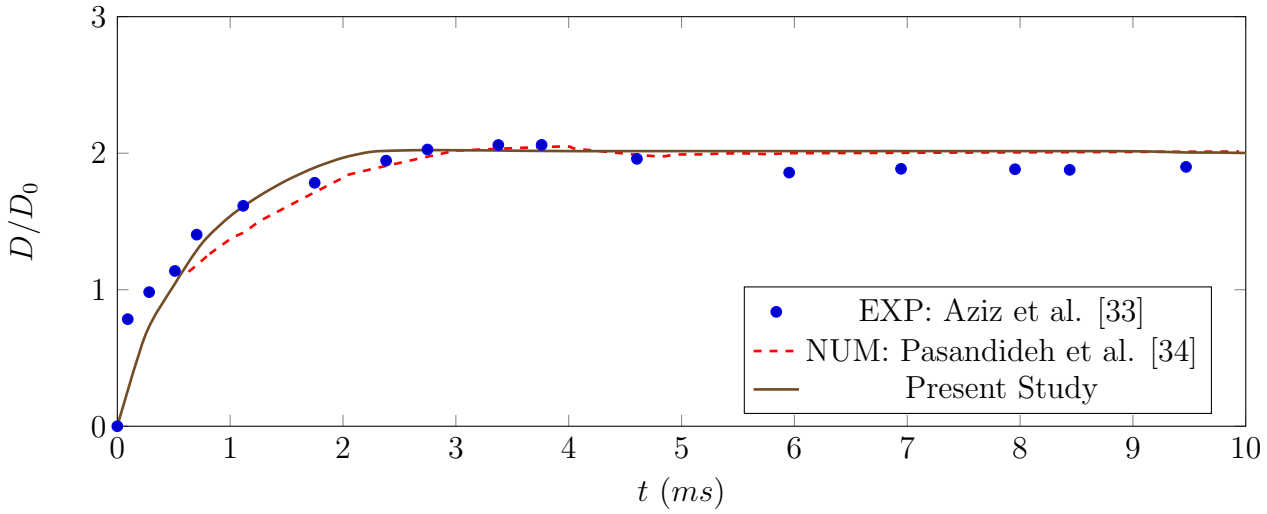

Figure 8: Spread factor (D/D_0) for a tin drop at 240°C with 2.7mm diameter impacting at 1m/s on a 25°C stainless steel substrate.

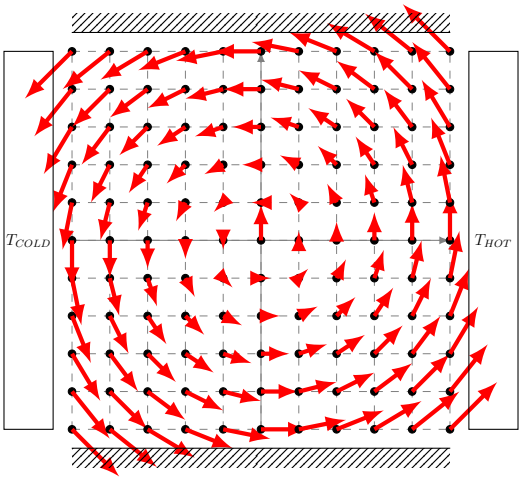

(a) Inital boundary conditions.

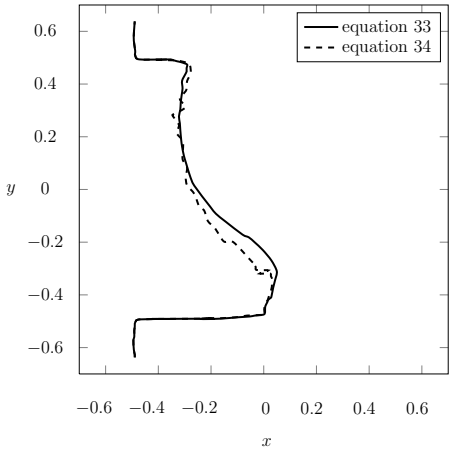

(b) Solidification front at $t = 0.16$.

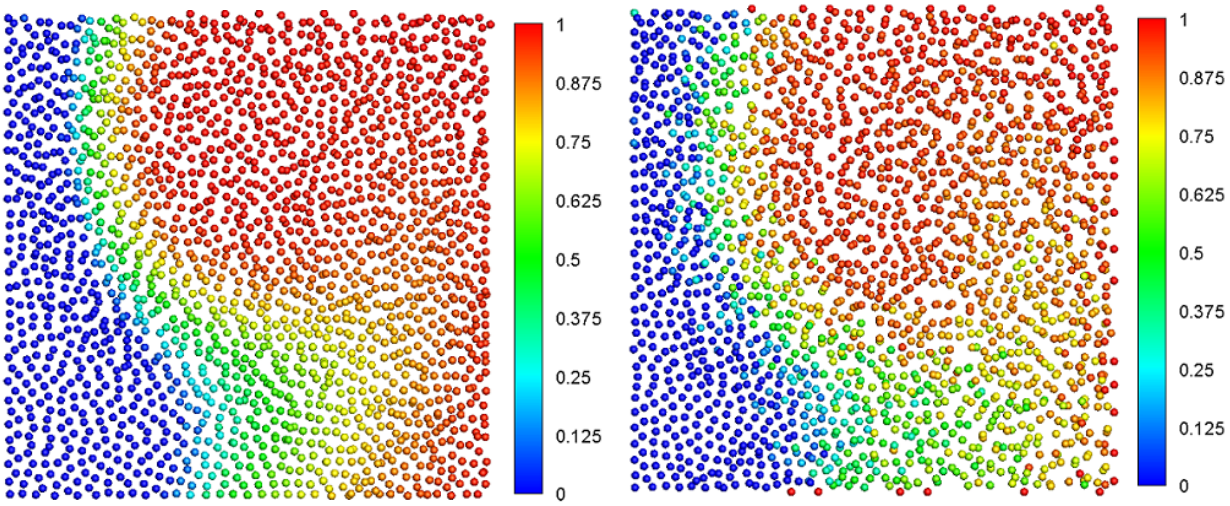

Using equation 33 Using equation 34

(c) Particle positions at $t = 0.16$ (s) colored by their liquid fractions.

Figure 9: Example of mushy zone effects inside a 1×1 rectangle domian.

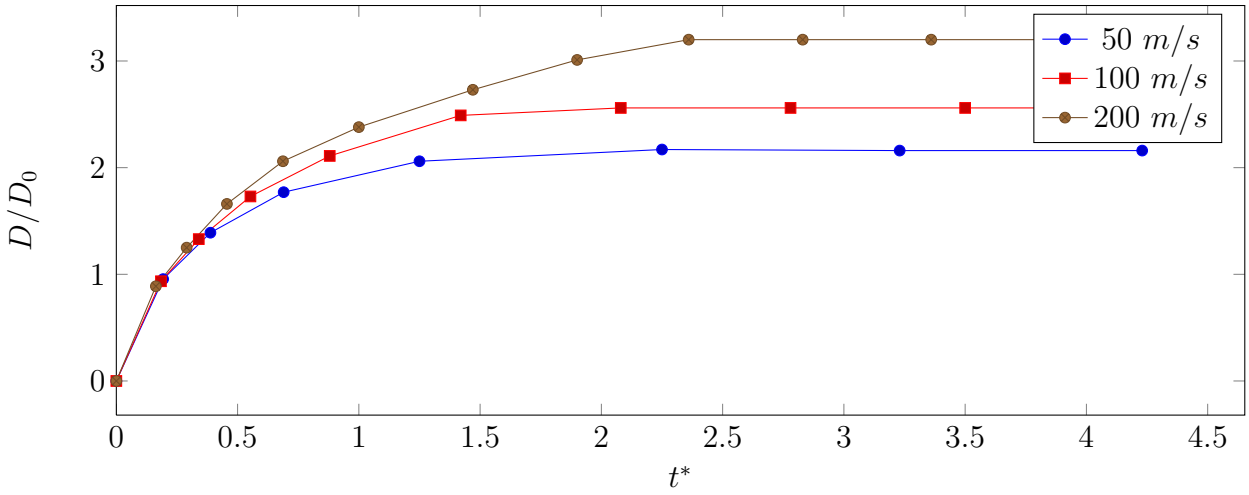

Figure 10: Spread factor (D/D_0) for a YSZ droplet impacting the substrate at 50, 100, and $200m/s$ ($t^* = tV/D_0$).

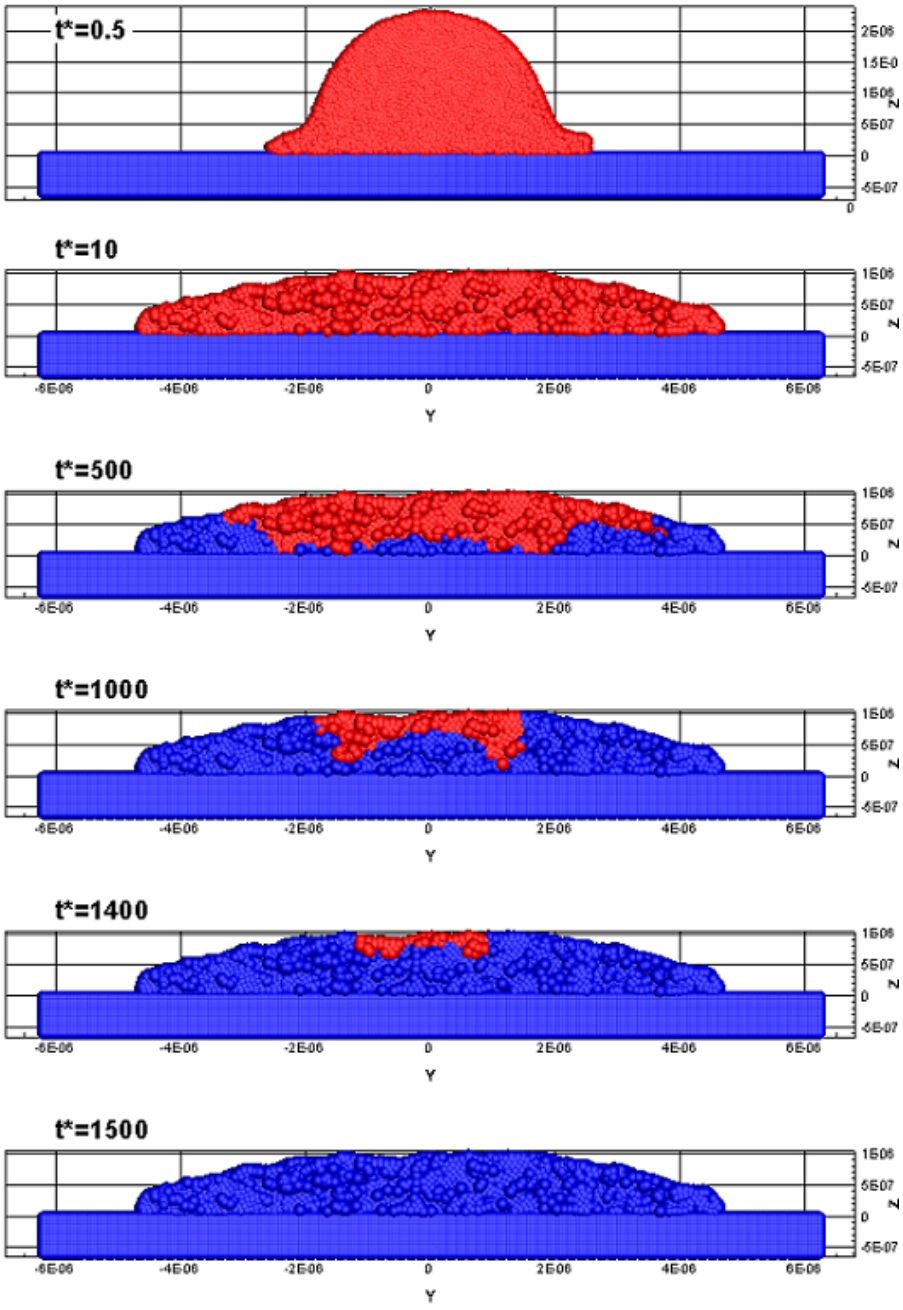

Figure 11: Impact and solidification time for a droplet at temperature of $3000K$ with radius of $3\mu m$ and velocity of $150m/s$.

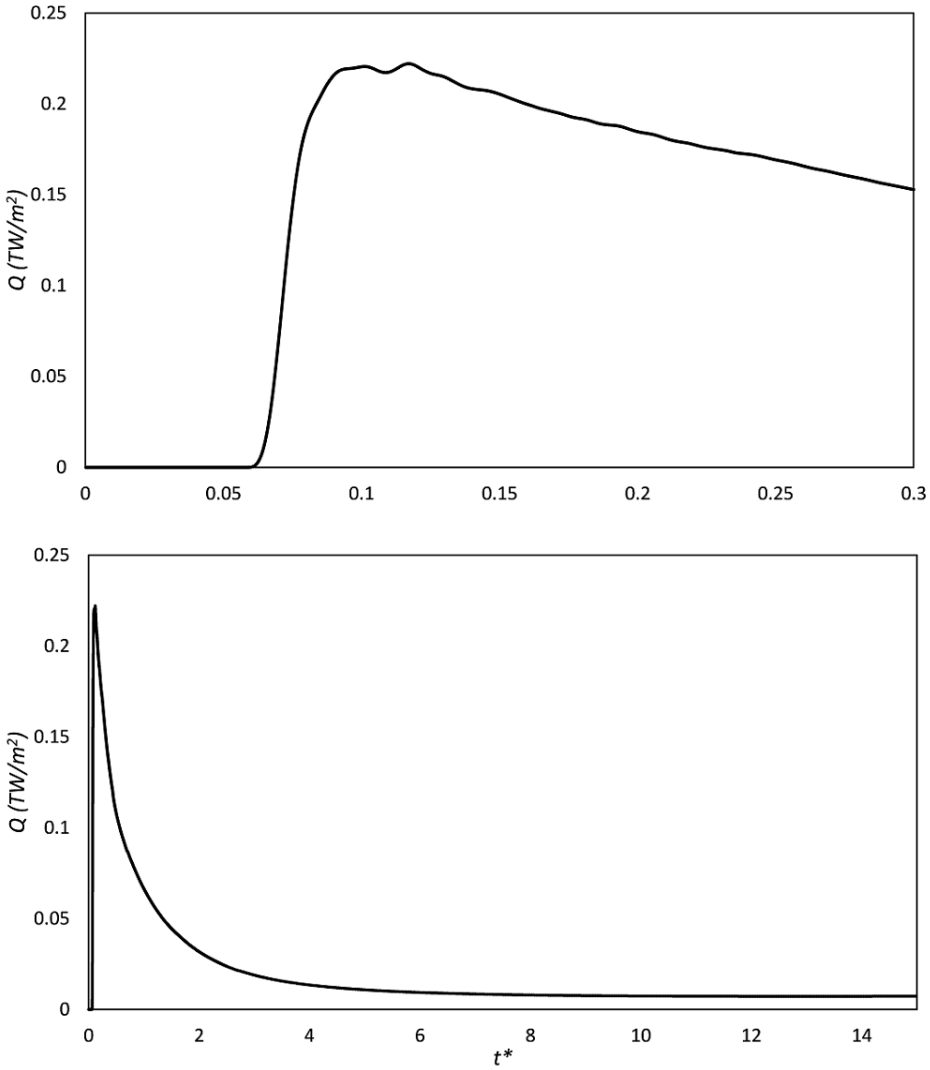

Figure 12: Heat flux at the impact point of the droplet on the substrate as a function of non-dimensional time ($t^* = tV/D_0$), shown near the time of impact (figure on top) and afterwards (figure on bottom).

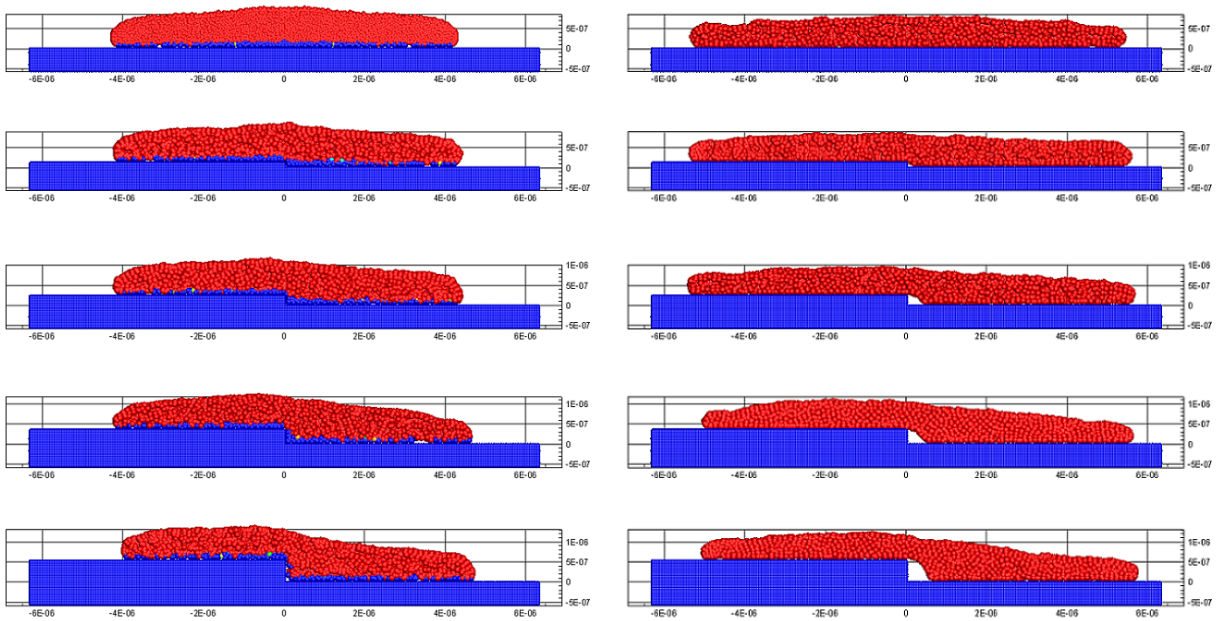

(a) Droplet initial temperature of $2985k$ (b) Droplet initial temperature of $3500k$

Figure 13: Normal impact of droplet with a radius of $3\mu m$ on flat surface against surfaces with step sizes of 0, 0.12, 0.24, 0.36, and $0.54\mu m$, from top to bottom respectively. Impact velocity is $150m/s$ and substrate temperature is $300K$ and $t = 0.1\mu s$.

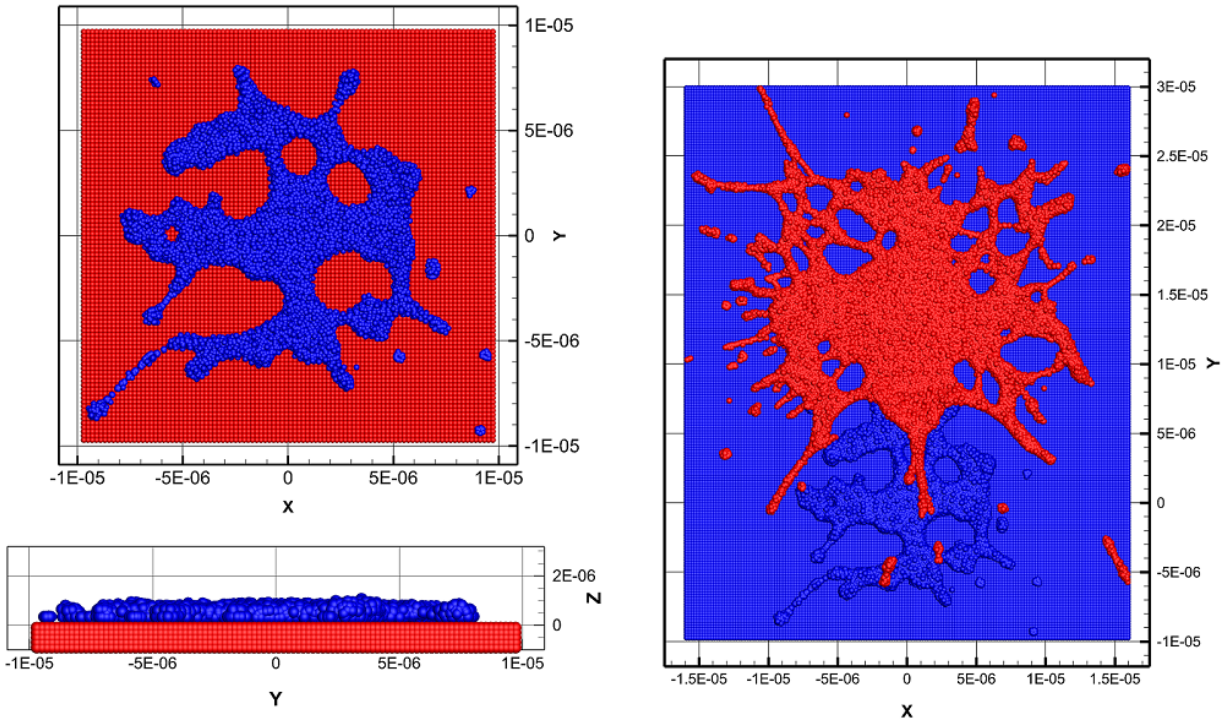

(a) (b)

Figure 14: Binary impact of droplets with diameters of 4.59 and 6.8μm at velocities of 175 and 231m/s and temperature of 3517 and 3795K, respectively. The position of impact is offset by 14μm.

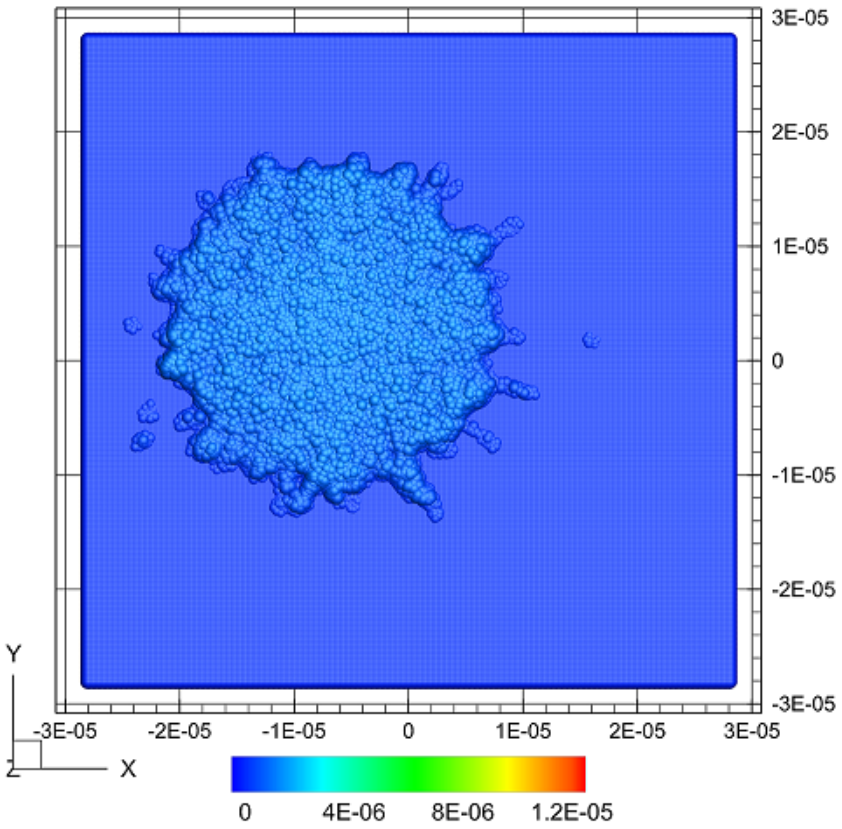

(a)

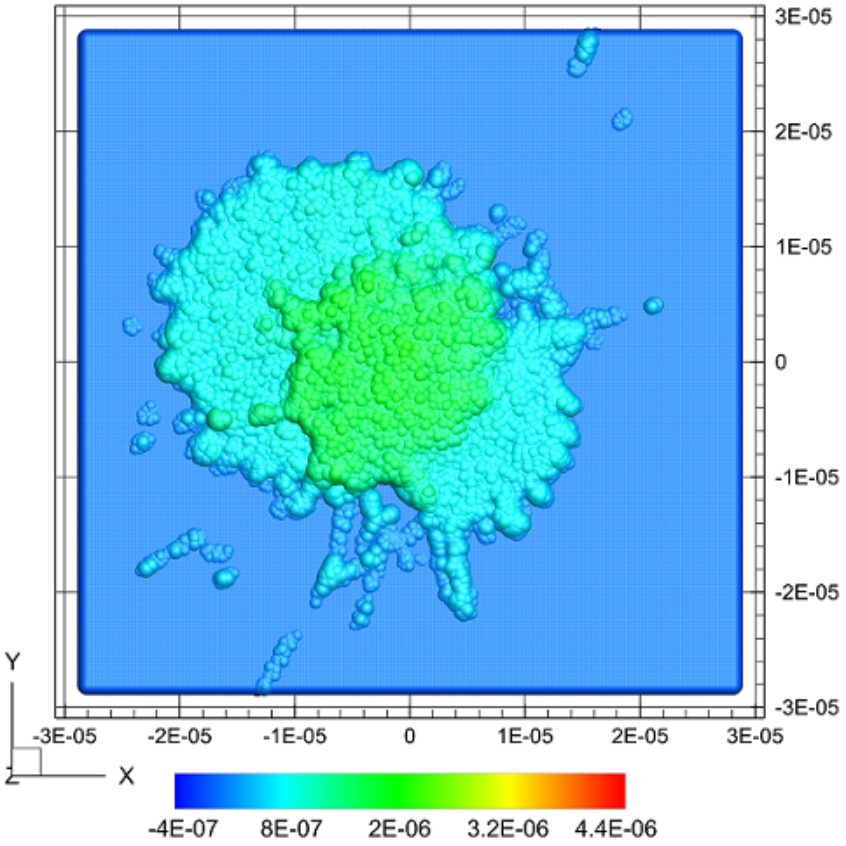

(b)

Figure 15: Solidified splats of droplets #1 and #2 from table 2, colored by height from the substrate.

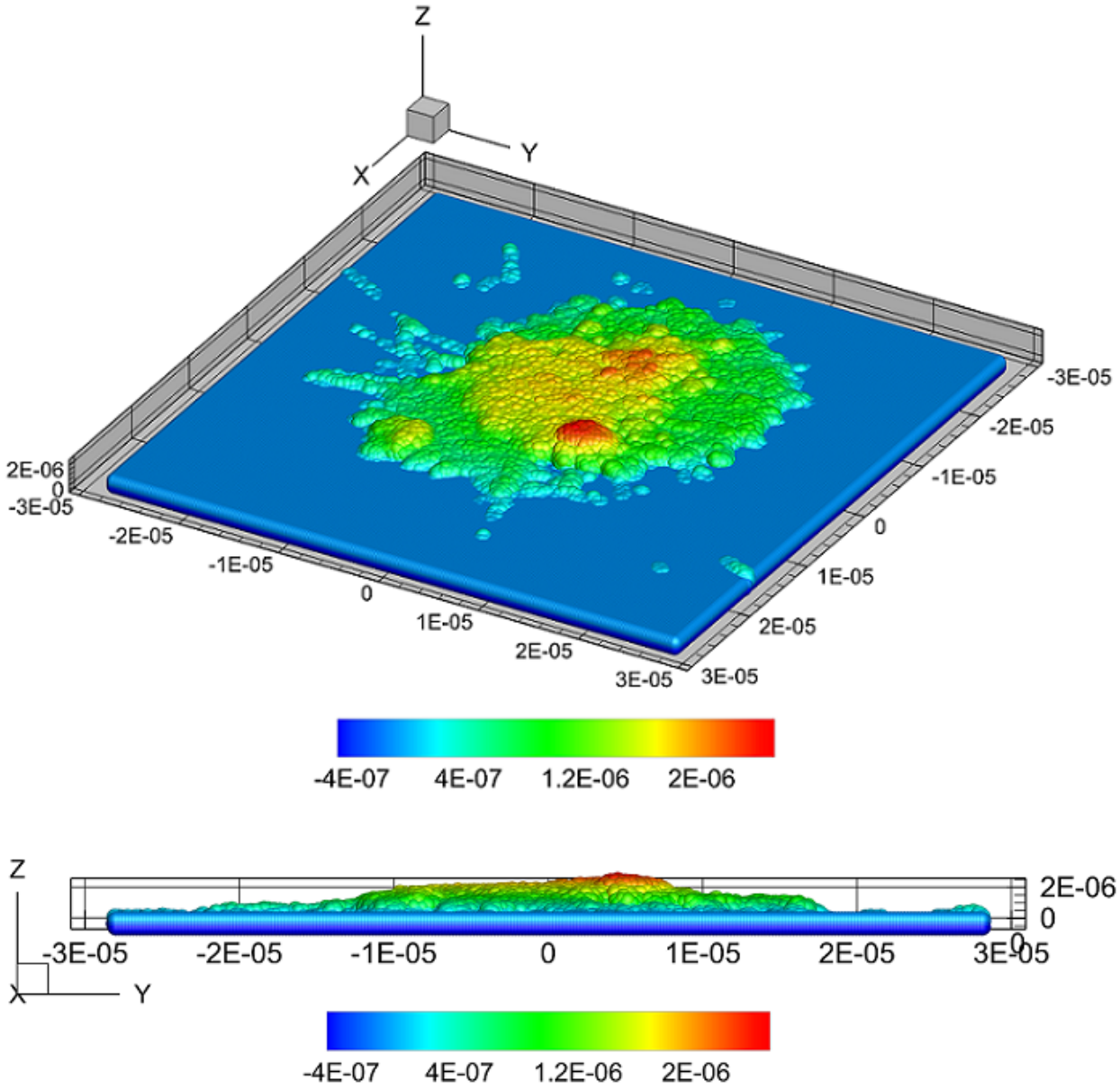

Figure 16: Solidified splats of droplets #1-#5 from table 2, colored by height from the substrate.

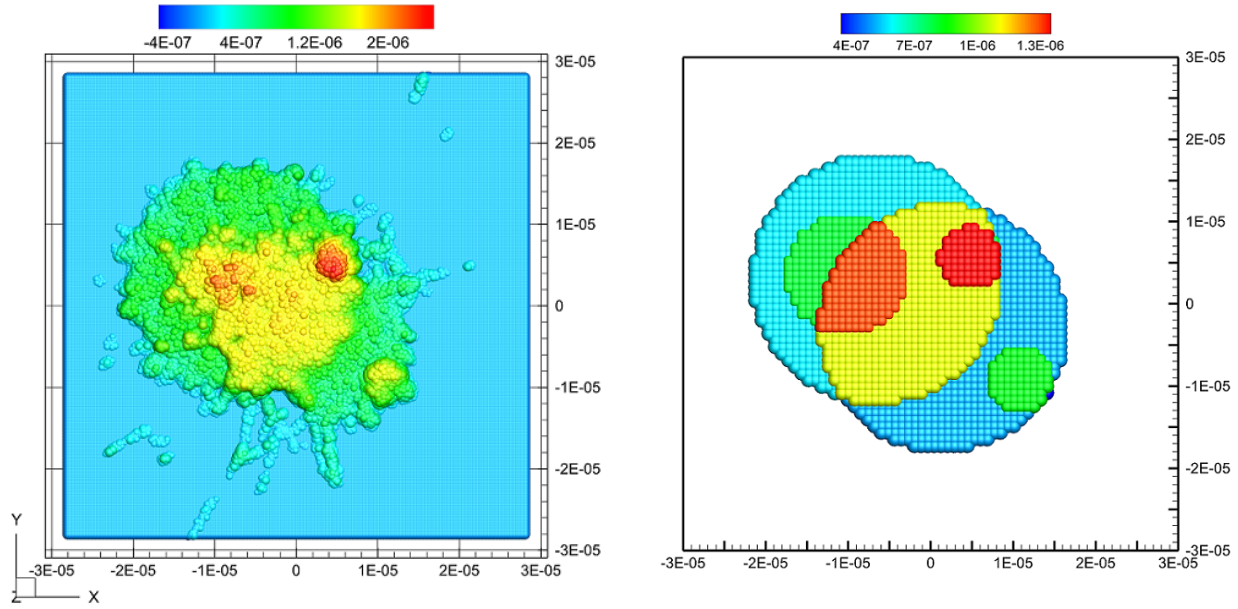

(a) For five splats of table 2

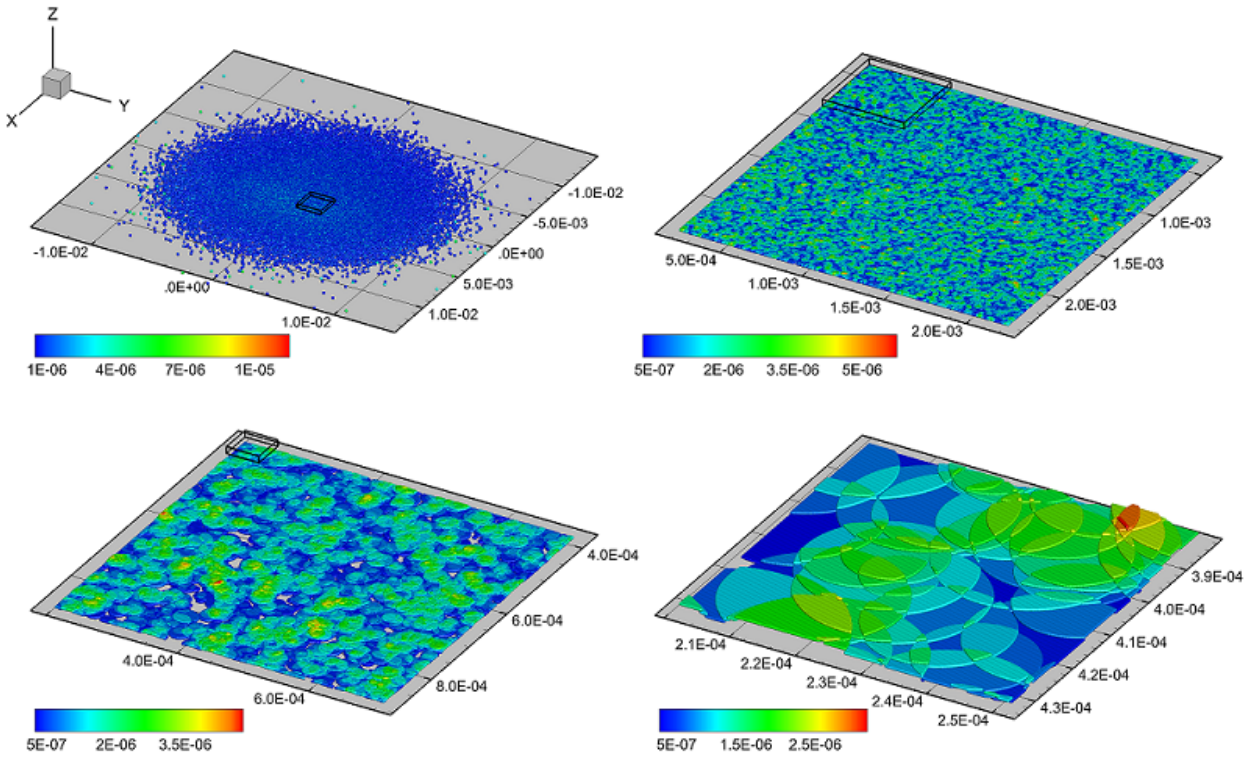

(b) For 1 million splats obtained from SPS data

Figure 17: Substrate coverage estimated by overlapping discs.

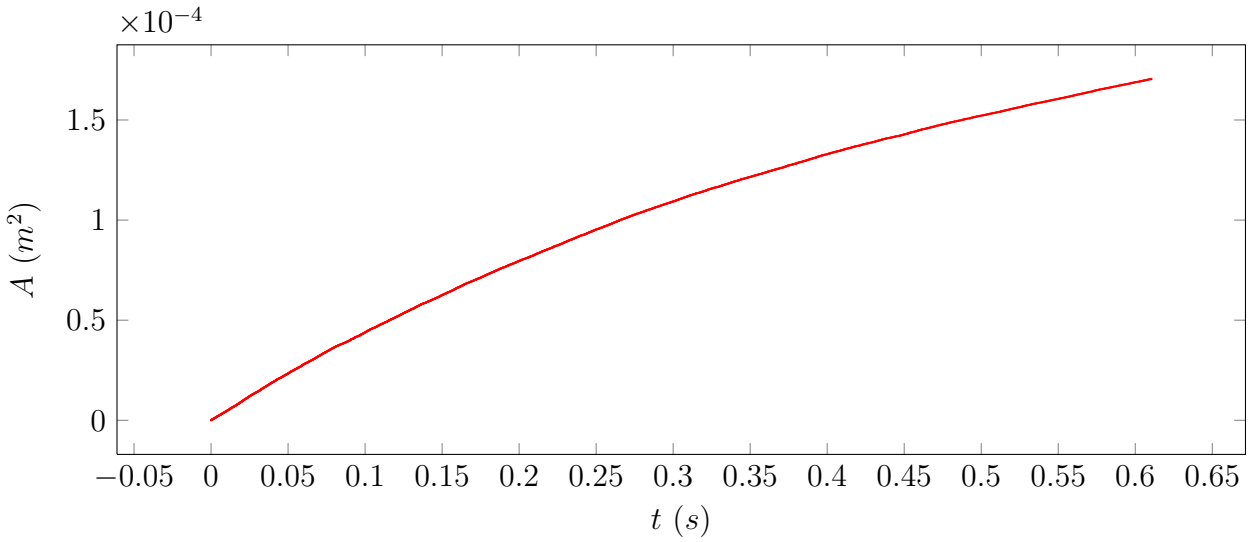

Figure 18: Growth of the area of the solidified material on the substrate as a function of time for 1 million splats obtained from SPS data.